https://doi.org/10.5194/egusphere-2026-1619
Preprint. Discussion started: 6 May 2026

A new Monte Carlo treatment of multiple scattering of light by black carbon aggregates with varying levels of compactness

Ynon Hefets and Carynelisa Haspel
Fredy and Nadine Herrmann Institute of Earth Sciences, The Hebrew University of Jerusalem, Jerusalem, Israel
Correspondence to: Ynon Hefets (ynon.hefets@mail.huji.co.il)

Abstract.

We use a specially designed Monte Carlo (MC) model that includes individual Mueller matrix selection in each scattering event to conduct a comprehensive theoretical investigation of the intensity and polarization of light multiply scattered by an atmospheric layer embedded with black carbon (BC) particles with varying compactness. We find that the spatial distributions of the degree of linear and circular polarization are sensitive to BC particle shape, and that depolarization is more dominant for spherical BC particles than for fractal aggregates. We also find that the layer transmittance is highest for the more spherical BC particle shapes and lowest for the extended fractal aggregates, with an overall difference of approximately 10% relative to the incident intensity between the highest and lowest values of transmittance. We find that the reflectance exhibits a similar tendency, and that correspondingly, the layer absorptance is lowest for the more spherical BC shapes and highest for the extended fractal aggregates. In addition, we compare the results obtained from our MC simulations with those obtained with the delta-Eddington approximation for the same optical thickness, single scattering albedo, asymmetry factor, and incident zenith angle. We find that there is a relatively small difference between our results and the delta-Eddington results with respect to the layer transmittance and the layer absorbance, but that the layer reflectance obtained with our MC simulations is up to 50% lower than that obtained with the delta-Eddington approximation. These results could have important implications for radiative forcing estimations, climate modeling, and remote sensing implementations.

1 Introduction

Atmospheric aerosol particles labeled as black carbon (BC), element carbon (EC), light absorbing carbon (LAC), or soot are important components of Earth's atmosphere to consider; they are pollutants and also affect atmospheric chemistry, cloud formation, the climate, and remote sensing efforts. As such, their properties, in particular their scattering and absorption properties, have been investigated in many previous studies. See, for example, the single scattering results presented in Bond et al. (2006), Liu and Mishchenko (2005, 2007), Liu et al. (2008), Soewono and Rogak (2013), Romshoo et al. (2021, 2022) and the comprehensive papers by Bond and Bergstrom (2006), Liu and Mishchenko (2018), and Kahnert and Kanngießer (2020). Such particles (hereafter "BC") often occur in aggregate structures with various levels of compactness and are often categorized as such using fractal parameters. As the aforementioned papers and references therein point out, the unique

https://doi.org/10.5194/egusphere-2026-1619
Preprint. Discussion started: 6 May 2026

structure of BC particles can strongly affect the scattering and absorption properties of BC particles with respect to solar radiation.

In addition to their effect on the intensity of scattered solar radiation, aerosol and hydrosol particles in general and BC particles in particular can affect the polarization (the orientation of the electric or magnetic field) of scattered solar radiation. (See, e.g., Ugolnikov et al., (2004), Liou et al., (2013), Han et al., (2021), as well as the aforementioned references). Polarization states include unpolarized radiation, linear polarization (LP), circular polarization (CP), and elliptical polarization, the last of which is any combination of LP and CP. In addition to the type of polarization, the degree of polarization (DoP; ranging from 0 to 1) and the angle of polarization can be specified for any partially to fully polarized wave of electromagnetic radiation and can be specified separately for linear and circular polarization (DoLP and DoCP, respectively). Scattering can create polarization (can convert unpolarized radiation into partially or fully polarized radiation, i.e., can increase the DoP) or conversely, scattering can cause depolarization (can convert fully polarized radiation into partially polarized or unpolarized radiation, i.e., can decrease the DoP). Moreover, scattering can influence the persistence of a polarized radiation state as it propagates through the scattering layer. For example, circularly polarized light has been shown to exhibit more persistence than linearly polarized light in environments with forward-scattering particles (Xu and Alfano 2005; van der Laan et al. 2015 and references therein; Zhang et al. 2020 and references therein). Given all of the above, the ability to model the propagation of solar radiation, considering both the intensity and polarization of the radiation under multiple scattering, is important. Moreover, a proper description of the intensity and polarization of solar radiation under multiple scattering can be useful in in remote sensing applications (see, e.g., Quinby-Hunt et al. (1997), Quinby-Hunt et al. (2000), Chami et al. (2001; 2015), Tyo et al. (2006), Koestner et al. (2020), Gassó and Knobelspiesse (2022), and references therein.)

In a relatively recent study (Haspel et al. (2023)), it was found that not only are the particulars of the aggregate structure important but also assumptions concerning the orientation of the particles with respect to an incident electromagnetic wave. It was found that in computing the scattering and absorption by BC aggregates, when the commonly-used random orientation assumption is employed, the computed intensity of scattered radiation polarized perpendicular to the scattering plane and propagating into side- and back-scattering directions is not high enough as compared to the intensity measured in controlled laboratory measurements. It was found that certain aggregate shapes contribute adequately to the perpendicularly polarized scattered intensity and thus to the linear depolarization ratio only when allowing for fixed orientation but not with random orientation. The study by Haspel et al. (2023) has important implications for radiative transfer and remote sensing in the presence of BC particles, but it considered only single scattering by individual BC aggregates and not multiple scattering by a collection of such aggregates.

In the present study, we complement the study of Haspel et al. (2023) by conducting a comprehensive theoretical investigation of the intensity and polarization of radiation multiply scattered by a collection of BC aggregates using a specially designed

https://doi.org/10.5194/egusphere-2026-1619
Preprint. Discussion started: 6 May 2026

Monte Carlo (MC) model. To directly complement the results from Haspel et al. (2023), we use the same wavelength of incident radiation and include aggregate shapes with the same parameters as in that study. As we explain below, unique our MC model is designed to address the same fixed versus random orientation issue as explored in Haspel et al. (2023) and thus produces important intensity and polarization output under such scatterer conditions.

2 Methods

2.1 Black carbon scatterers

To simulate multiple scattering by BC aggregates, we adopt aggregate shapes from Haspel et al. (2023) spanning a broad range of aggregate shapes from compact aggregates to extended aggregates. These aggregate shapes were generated using the fractal aggregate generating code of Mackowski (1995, 2006) with 6 different sets of fractal parameters, i.e., 6 combinations of the 3D fractal dimension (D_f) and the fractal pre-factor (k_f): $D_\mathrm{f} = 2.34$, $k_\mathrm{f} = 1.08$; $D_\mathrm{f} = 2.16$, $k_\mathrm{f} = 2.06$; $D_\mathrm{f} = 2.56$, $k_\mathrm{f} = 1.19$; $D_\mathrm{f} = 1.92$, $k_\mathrm{f} = 1.87$; $D_\mathrm{f} = 1.68$, $k_\mathrm{f} = 1.69$; and $D_\mathrm{f} = 2.12$, $k_\mathrm{f} = 0.99$. For each set of fractal parameters, we generated 6 realizations, for a total of 36 aggregate realizations. For comparison, we also include results for highly compact, nearly spherical aggregates whose shapes were generated using the ideal amorphous solid (IAS) model of Stachurski (2003, 2011, and 2013), and for additional reference, we also include results for a homogeneous spherical scatterer computed using the Mie scattering algorithm presented in Bohren and Huffman (1983) and translated to the MATLAB computing language by Boss (1998). Each fractal aggregate and IAS aggregate that we generated consists of 771 monodisperse homogeneous spheres of radius of 17.5 nm as its constituent primary particles. The diameter of the Mie sphere, which is roughly 0.321 μm, is set such that the Mie sphere has an equal volume (and thus an equal mass) to the aggregates. Examples of each shape are shown in Fig. 1. As one can see from Fig. 1, the fractal aggregates in Figs. 1b-d are more compact, with that shown in Fig. 1d being the most compact with an almost spherical shape, and the fractal aggregates in Figs. 1f-h are more extended, with that shown in Fig. 1g being the most extended.

In preparation for the multiple scattering MC simulations, we pre-compute the single scattering properties of every aggregate realization using our discrete dipole approximation (DDA) model (Hefets and Haspel, 2023, 2025). The single scattering properties include: the single scattering albedo ϖ, the asymmetry factor g; and the 4×4 single scattering (Mueller) matrix $\mathbf{M}(\theta_\mathrm{sca}, \phi_\mathrm{sca})$, where θ_sca and ϕ_sca are the polar and azimuthal scattering angles. For each aggregate realization (for the IAS aggregate and for each of the 36 fractal aggregates), we pre-compute the Mueller matrix with 102 equally spaced orientations relative to the direction of the incident beam with a resolution of 1° in θ_sca and in ϕ_sca, respectively. Moreover, this resolution gives us the option of rotating the scatterer with respect to ϕ_sca in intervals of 1°, which gives us de facto 360×102 different orientations for each scatterer. In all of the above single scattering computations, as in Haspel et al. (2023), we set the wavelength to be $\lambda = 0.67$ μm, and we assign the scatterers a complex refractive index of $n = 1.85 + 0.71i$. The computed

https://doi.org/10.5194/egusphere-2026-1619
Preprint. Discussion started: 6 May 2026

single scattering albedo and asymmetry factor values are given in Table 1. The single scattering albedo values and the Mueller matrices are used directly in the MC simulations (see Sect. 2.2), while the asymmetry factor values are used along with the single scattering albedo values in analyzing the multiple scattering results and in comparing those results against conventional multiple scattering approximations (see Sect. 3).

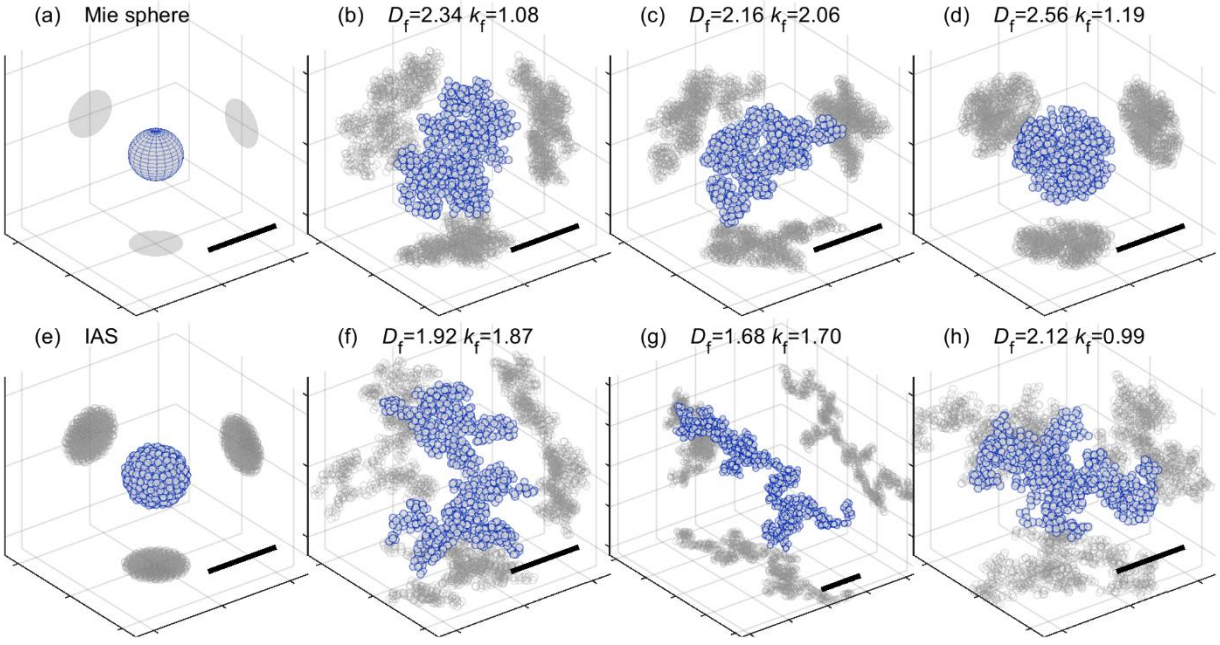

Figure 1. Examples of the BC scattering particles (and their projections). The scale-bar and grid size are 0.5 μm. Note that due to its very extended shape, the scale size of (g) is different from that of the other sub-figures.

	Single scattering albedo – ϖ	Asymmetry factor – g
Mie sphere	0.428	0.497
IAS aggregate	0.418±0.001	0.628±0.001
Fractal aggregate: $D_f = 2.34$, $k_f = 1.08$	0.276±0.013	0.744±0.027
Fractal aggregate: $D_f = 2.16$, $k_f = 2.06$	0.299±0.015	0.710±0.036
Fractal aggregate: $D_f = 2.56$, $k_f = 1.19$	0.336±0.008	0.724±0.025

https://doi.org/10.5194/egusphere-2026-1619
Preprint. Discussion started: 6 May 2026

Fractal aggregate: $D_f = 1.92$, $k_f = 1.87$	0.224±0.020	0.697±0.039
Fractal aggregate: $D_f = 1.68$, $k_f = 1.70$	0.156±0.019	0.641±0.054
Fractal aggregate: $D_f = 2.12$, $k_f = 0.99$	0.205±0.018	0.738±0.031

Table 1. Values of the single scattering albedo and asymmetry factor for the different shapes of the BC scattering particle. For the aggregates, the means (±1 standard deviation) are taken over the realizations and orientations of the aggregates.

2.2 Monte Carlo simulations with a unique treatment of scatterer orientation

The framework of our MC model is similar to the algorithm described in depth in Ramella-Roman et al. (2005). However, as mentioned in Sect. 1, based on the insights gained in Haspel et al. (2023), we treat the possible scatterer orientations in a unique way. Rather than using a Mueller matrix that has been pre-averaged over scatterer orientation (the conventional methodology for handling random orientation; see, e.g., Mishchenko et al. (2000)), in the present study, for each individual scattering event, we select the Mueller matrix for that event using specific selection rules, as we describe below. Our "individual Mueller matrix selection" method serves to better represent the situation encountered in Haspel et al. (2023), in which each individual BC scattering particle produces scattered intensity based on its individual orientation at the moment of a given scattering event. Moreover, from preliminary simulations (see Appendix A), we found that the difference of the scattering angle distribution between our individual Mueller matrix selection method and the conventional pre-averaged Mueller matrix method is not negligible, with relative differences between the two methods reaching ~5% over a large span of scattering angles in both forward and backward propagation directions in the case of more extended fractal aggregates.

The model is coded in MATLAB and is set up for parallel processing on multiple CPUs. In each simulation, a beam of 10^7 photons is launched from the origin into a plane-parallel atmospheric layer with a specified optical thickness, τ^*; see Fig. 2. For convenience, the distance transversed by a photon is represented in units of optical depth, $\tau = r\mu_{\text{ext}}$, where r is the geometric distance, and μ_{ext} is the extinction coefficient. In each simulation, the atmospheric layer contains a collection of scatters all of which have one BC particle shape; if that shape is one of the 6 fractal aggregate shapes, all 6 realizations of that shape are included and are selected randomly along with the aggregate orientation for each individual scattering event.

In a given simulation, all of the photons are initialized with an identical wave vector, $\boldsymbol{k}_n = (k_x, 0, -k_z)' = (\sin\theta_{\text{zen}}, 0, -\cos\theta_{\text{zen}})'$, where θ_{zen} is the (zenith) angle relative to the normal of the surface of the scattering layer, and with an identical polarization, defined by their Stokes vector $\boldsymbol{S}_n = (I_n, Q_n, U_n, V_n)'$, where I_n, Q_n, U_n, and V_n are the Stokes parameters of the n^{th} photon. The prime symbols indicate that the vectors are column vectors. By default, the initial intensity of the incident photons is set to be a unitless value of 1. Each photon propagates a distance s in optical depth calculated as

https://doi.org/10.5194/egusphere-2026-1619
Preprint. Discussion started: 6 May 2026

$$s = -\ln(1-u), \tag{1}$$

where u is a random number with a uniform distribution between 0 and 1, before interacting with a scatterer.

The interaction proceeds as follows. If the scatterer is a fractal aggregate, then first, one of the 6 possible aggregate realizations for that aggregate is selected from a uniform random integer distribution between 1 and 6. Next, one of the 102 equally spaced possible aggregate orientations is selected from a uniform random integer distribution between 1 and 102, and one of the 360 equally spaced possible azimuthal angles of the scatterer relative to the incident direction of the photon is selected from a uniform random integer distribution between 1 and 360. The probability of the radiation being scattered into the θ_{sca}, ϕ_{sca} direction is dictated by the discrete scattering probability function (also known as the scattering phase function):

$$P(\theta_{\text{sca}}, \phi_{\text{sca}}) = \frac{\tilde{I}(\theta_{\text{sca}}, \phi_{\text{sca}})}{\sum_{l=0}^{180}\sum_{m=0}^{359} \tilde{I}(\theta_{\text{sca}}, \phi_{\text{sca}})\Delta\Omega_{\text{lm}}}, \tag{2}$$

where:

$$\tilde{I}(\theta_{\text{sca}}, \phi_{\text{sca}}) = M_{11}(\theta_{\text{sca}}, \phi_{\text{sca}})I_n + M_{12}(\theta_{\text{sca}}, \phi_{\text{sca}})[\cos(2\phi_{\text{sca}})\, Q_n + \sin(2\phi_{\text{sca}})\, U_n] +$$

$$M_{13}(\theta_{\text{sca}}, \phi_{\text{sca}})[\cos(2\phi_{\text{sca}})\, U_n - \sin(2\phi_{\text{sca}})\, Q_n] + M_{14}(\theta_{\text{sca}}, \phi_{\text{sca}})V_n, \tag{3}$$

and $\Delta\Omega$ is the discrete unit of solid angle. In accordance with its definition in Eq. 2, the scattering probability function is normalized such that $\sum_{l=0}^{180}\sum_{m=0}^{359} P(\theta_l, \phi_m)\Delta\Omega_{\text{lm}} = 1$. The new scattering direction is chosen using the rejected method. First, a possible value of θ_{sca} is chosen randomly from a uniform integer distribution between 0 and 180 and is set as θ_{rand}. Next, a possible value of ϕ_{sca} is chosen randomly from a uniform integer distribution between 1 and 360 and is set as ϕ_{rand}. Then, a third random number, p_{rand}, is chosen from a uniform real number distribution between 0 and $P_{\text{max}} = \max[P(\theta_{\text{sca}}, \phi_{\text{sca}})\Delta\Omega]$. If $P(\theta_{\text{rand}}, \phi_{\text{rand}})\Delta\Omega \geq p_{\text{rand}}$, then θ_{rand} and ϕ_{rand} are accepted as the values of θ_{sca} and ϕ_{sca}, respectively, for the scattering event. If $P(\theta_{\text{rand}}, \phi_{\text{rand}})\Delta\Omega < p_{\text{rand}}$, then the scattering direction is rejected, and a new set of random values are drawn and tested. For a more detailed description of the rejection method, see Bartel and Hielscher (2000) and Ramella-Roman et al. (2005). After choosing the scattering direction, the scattered Stokes vector for the scattering event is calculated as:

$$\boldsymbol{S}_{n,\text{sca}} = \mathbf{M}(\theta_{\text{sca}}, \phi_{\text{sca}})\mathbf{R}(\phi_{\text{sca}})\boldsymbol{S}_{n,\text{inc}}, \tag{4}$$

https://doi.org/10.5194/egusphere-2026-1619
Preprint. Discussion started: 6 May 2026

where $\boldsymbol{S}_{n,\mathrm{inc}}$ is the incident Stokes vector, $\boldsymbol{S}_{n,\mathrm{sca}}$ is the scattered Stokes vector, and $\mathbf{R}(\phi_{\mathrm{sca}})$ is the rotation matrix, rotating the linear polarization coefficient Q_n and U_n to the new scattering plane of the photon:

$$\mathbf{R}(\phi_{\mathrm{sca}}) = \begin{pmatrix} 1 & 0 & 0 & 0 \\ 0 & \cos(2\phi_{\mathrm{sca}}) & \sin(2\phi_{\mathrm{sca}}) & 0 \\ 0 & -\sin(2\phi_{\mathrm{sca}}) & \cos(2\phi_{\mathrm{sca}}) & 0 \\ 0 & 0 & 0 & 1 \end{pmatrix}. \quad (5)$$

To account for energy loss due to absorption by the BC particles, in each scattering event, the scattered Stokes vector is normalized such that $I_{n,\mathrm{sca}} = \varpi I_{n,\mathrm{inc}}$, where I_n is the first element of the Stokes vector, respectively, and represents the radiative intensity of the photon, and ϖ is the single scattering albedo pre-computed for the specific realization and orientation of the chosen scatterer as described in Sect. 2.1. In this way, a given photon is not only scattered into a new direction as a result of each scattering event but also loses intensity due to absorption as a function of the number of scattering events: $I_{n,j} = \prod_{j=1} \varpi_j$, where j is the scattering event number. The Stokes vector after j scattering events is:

$$\boldsymbol{S}_{n,j} = \begin{pmatrix} I_{n,j} \\ Q_{n,j} \\ U_{n,j} \\ V_{n,j} \end{pmatrix} = \prod_{j=1} \varpi_j \begin{pmatrix} 1 \\ q_{n,j} \\ u_{n,j} \\ v_{n,j} \end{pmatrix} \quad (6)$$

The photon continues its trajectory through the scattering layer with its succession of scattering events until it leaves the layer in the forward (transmitted) direction (red curves in Fig. 2a) or in the backward (reflected) direction (green curves in Fig. 2a), or until it is absorbed inside the layer (blue curves in Fig. 2a); absorption of a photon is manifested when its intensity drops below a threshold set as (the unitless value of) 10^{-4}.

During each individual scattering event, the Stokes coefficients Q_n and U_n are computed with respect to the individual scattering plane of the event, i.e., the plane defined by the incident wave vector of the photon before the event and the scattered wave vector of the photon after the event. Once a photon leaves the scattering layer, the final scattering plane of the photon is rotated such that it coincides with the horizontal (XZ) plane in the laboratory frame. In this way, in the resultant Stokes vector, $Q_n = 1$ when the polarization is parallel to the horizontal (XZ) plane, and $Q_n = -1$ when the polarization is parallel to the vertical (YZ) plane (see Fig. 2b). For more details on the rotation of the scattering plane, see the description of the Euler MC method in Ramella-Roman et al. (2005).

https://doi.org/10.5194/egusphere-2026-1619
Preprint. Discussion started: 6 May 2026

In a given simulation, all of the photons are initialized with the identical initial polarization, which is LP, CP, or unpolarized. For incident LP with incident zenith angle 0°, without loss of generality, we set the initial LP orientation to be parallel to the scattering plane ($Q_n = 1$). For incident LP and incident zenith angles other than 0°, we conducted a pair of simulations, one with the initial LP oriented parallel to the scattering plane ($\mathrm{LP}_{\parallel}$, $Q_n = 1$) and one with the initial LP oriented perpendicular to the scattering plane ($\mathrm{LP}_{\perp}$, $Q_n = -1$). For incident CP, again without the loss of generality, we set the initial CP to be right circularly polarized. Thus, in a given simulation, the initial Stokes vector of all of the photons is set to one of the following:

$$\boldsymbol{S}_{\mathrm{LP,LP}_{\parallel}} = \begin{pmatrix} 1 \\ 1 \\ 0 \\ 0 \end{pmatrix}, \boldsymbol{S}_{\mathrm{LP}_{\perp}} = \begin{pmatrix} 1 \\ -1 \\ 0 \\ 0 \end{pmatrix}, \boldsymbol{S}_{\mathrm{CP}} = \begin{pmatrix} 1 \\ 0 \\ 0 \\ 1 \end{pmatrix}, \boldsymbol{S}_{\mathrm{UNP}} = \begin{pmatrix} 1 \\ 0 \\ 0 \\ 0 \end{pmatrix}, \tag{7}$$

where "UNP" stands for unpolarized.

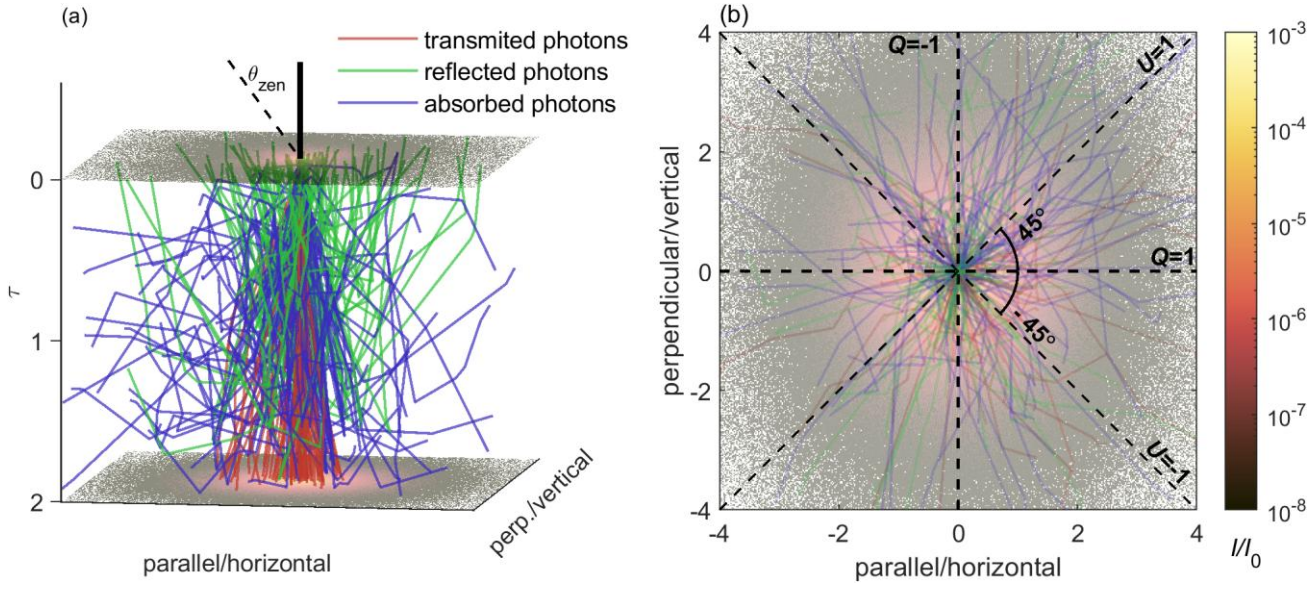

Figure 2. Side (a) and top (b) view of the forward and backward scattering intensity and of the propagation paths of 300 photons propagating from an incident zenith angle of $\theta_{\mathrm{zen}} = 0°$ in an atmospheric layer of containing BC particles shaped as fractal aggregates with $D_{\mathrm{f}} = 2.34$ and $k_{\mathrm{f}} = 1.085$ and optical thickness $\tau^* = 2$. The incident polarization is linear and is oriented parallel to the horizontal axis. In (b), the intensity is the forward scattered intensity only, and the dashed lines indicate the orientation of the Stokes parameter in the laboratory frame.

2.3 Analyzing the output of the multi scattering simulations

In analyzing the output of the MC simulations, we present two types of results. The first type of result (presented in Sect. 3.1) includes the total transmittance (T), total reflectance (R), and total absorptance (A) of the atmospheric layer:

https://doi.org/10.5194/egusphere-2026-1619
Preprint. Discussion started: 6 May 2026

(8)

$$T = \frac{1}{I_0} \sum_{n,\text{forward}} I_n\,, \qquad R = \frac{1}{I_0} \sum_{n,\text{backward}} I_n,$$

and

$$A = 1 - T - R. \tag{9}$$

The summation is over all of the photons that either forward-scattered or backscattered from the layer, and I_0 is the incident intensity. T includes the photons that propagated directly through the layer without any interaction with the BC scatterers, in addition to the forward scattered photons. The second type of result (presented in Sects. 3.2 and 3.3), is a set of maps of the spatial distributions of the intensity, the DoLP, the DoCP, and the orientation of the polarization of forward and backward scattered light. To generate such maps, we keep track of the locations of the forward scattered photons on the back (the exit) surface of the layer and the locations of the backward scattered photons on the front (the entrance) surface of the layer. Then we divide each surface into small pixels of size of 0.02τ, $\times 0.02\tau$, and we compute the intensity and Stokes parameters of each pixel:

$$I_{\text{pix}} = \textstyle\sum_n I_n\,, \quad Q_{\text{pix}} = \frac{1}{I_{\text{pix}}} \textstyle\sum_n Q_n\,, \quad U_{\text{pix}} = \frac{1}{I_{\text{pix}}} \textstyle\sum_n U_n\,, \quad V_{\text{pix}} = \frac{1}{I_{\text{pix}}} \textstyle\sum_n V_n. \tag{10}$$

The DoLP and DoCP of each pixel are given by:

$$\text{DoLP}_{\text{pix}} = \sqrt{Q_{\text{pix}}^2 + U_{\text{pix}}^2}, \quad \text{DoCP}_{\text{pix}} = \left|V_{\text{pix}}\right|. \tag{11}$$

The orientation of the polarization, or the angle of linear polarization (AoLP) relative to the parallel/horizontal axis, is given by (see Fig. 2(b)):

$$\text{AoLP}_{\text{pix}} = \frac{1}{2} \tan^{-1}\left(\frac{U_{\text{pix}}}{Q_{\text{pix}}}\right). \tag{12}$$

Note that the range of the AoLP is $[-90°, 90°]$.

https://doi.org/10.5194/egusphere-2026-1619
Preprint. Discussion started: 6 May 2026

At this point, one may ask why not analyze the composite polarization properties of the transmitted and reflected light from the entire layer? There are two reasons for this. First, when inspecting the Stokes parameters of the surface of a layer, for example for incident CP, the Q and U parameters have positive and negative values in different regions of surface. When summing over all surface pixels, those opposite values nearly cancel one another, and the resulting DoLP of the entire layer comes out to be approximately zero. (In Sects. 3.2 and 3.3, we show that this approximately zero result is far from accurate). Secondly, when dealing with remote sensing of an atmospheric layer, it is not only the total values of the polarization that we are interested in, but also their distribution in space.

3. Results

3.1 Transmittance, reflectance and absorptance of an atmospheric layer embedded with BC scatterers

The variation of the transmittance, reflectance, and absorption of unpolarized light with different incident zenith angles propagating through an atmospheric layer embedded with BC scattering particles, as function of layer optical thickness is shown in Fig. 3. Overall, we can see that the transmittance, reflectance, and the absorptance vary over the different scatterer shapes despite the fact that they all have the same volume and hence mass of material (refer to Sect. 2.1), and this variation increases with incident zenith angle. As expected from their relatively higher single scattering albedo and lower asymmetry factor (refer to Table 1), the spherical scatterers (the Mie sphere and the IAS aggregate) produce both the highest transmittance and the highest reflectance of all of the scattering particle shapes for any optical thickness and incident zenith angle, and therefore, they produce the lowest absorption. (For incident zenith angles of 0° and 30°, the transmittance of the most compact fractal aggregate is approximately equal to the transmittance of the Mie sphere, but its reflectance is lower than that of the Mie sphere for all incident zenith angles). The more extended fractal aggregates (with D_f equal to 1.68, 2.12, and 1.92), which have the lowest single scattering albedo values (again, refer to Table 1), produce the lowest transmittance and reflectance, respectively, and consequently, they produce the highest absorption. For layers with an optical thickness between 0.5 and 2, the gap between the highest and the lowest transmittance or absorptance for the different particles is ~7-12% (relative to the incident intensity, i.e., $\sim 0.07I_0 - 0.12I_0$), for all incident zenith angles. For higher incident zenith angles, the reflectance produced by the Mie sphere and the IAS aggregate increases as well, from 3.2% and 1.5% for $\theta_{zen} = 0°$ up to 5.8% and 7.7% for $\theta_{zen} = 60°$, respectively. For the fractal aggregates, there is a much more moderate increase in the reflectance with incident zenith angle, but the reflectance is higher for the more compact aggregates relative to the more extended aggregates, especially at $\theta_{zen} = 60°$.

To evaluate the difference between our resulting transmittance, reflectance, and absorptance values and the transmittance, reflectance, and absorptance values that would be obtained using one of the conventional approximation techniques (the delta-Eddington approximation; Joseph et al., 1976) that are typically used in large scale (climate or global circulation) models (See,

https://doi.org/10.5194/egusphere-2026-1619
Preprint. Discussion started: 6 May 2026

e.g., Wiscombe and Evans, 1977, Leighton, 1980, Briegleb, 1992, and Freidenreich and Ramaswamy, 1999), in Fig. 4, we present plots of the relative difference:

$$\delta x = 2\frac{x_{\mathrm{MC}-} - x_{\delta-\mathrm{Edd}}}{x_{\mathrm{MC}+} + x_{\delta-\mathrm{Edd}}}, \tag{13}$$

where x is T, R, or A, respectively. Surprisingly, we find that the relative differences between our MC simulations and the delta-Eddington approximation are higher for the shapes that are isotropic with respect to ϕ_{sca}, i.e., for the Mie sphere and the IAS aggregate, and the relative differences between our MC simulations and the delta-Eddington approximation are lower for that shapes that are not isotropic with respect to ϕ_{sca}, i.e., for the fractal aggregates. It is surprising, because implementing the delta-Eddington approximation implicitly assumes isotropy of each scattering event with respect to ϕ_{sca} (see again, e.g., Joseph et al., 1976). The differences in transmittance and absorptance between our MC simulations and the delta-Eddington approximation are rather small, particularly when considering their absolute intensity, and they increase with increasing incident zenith angle. The differences in absorptance are only significant for layers with optical thicknesses less than one. In addition, the differences in the absorptance have a positive sign, which means that the MC simulations predict slightly higher absorptance than the delta-Eddington approximation predicts. Although the absolute intensity of the reflected light is relatively small ($\leq 0.075 I_0$), the relative difference in the reflectance is large, and its sign is negative, i.e., our MC simulations predict lower reflectance than the delta-Eddington approximation predicts. Both the higher absorptance and lower reflectance predicted by our MC simulations have potentially important implications for predicting absorption by BC particle layers in large scale models.

https://doi.org/10.5194/egusphere-2026-1619
Preprint. Discussion started: 6 May 2026

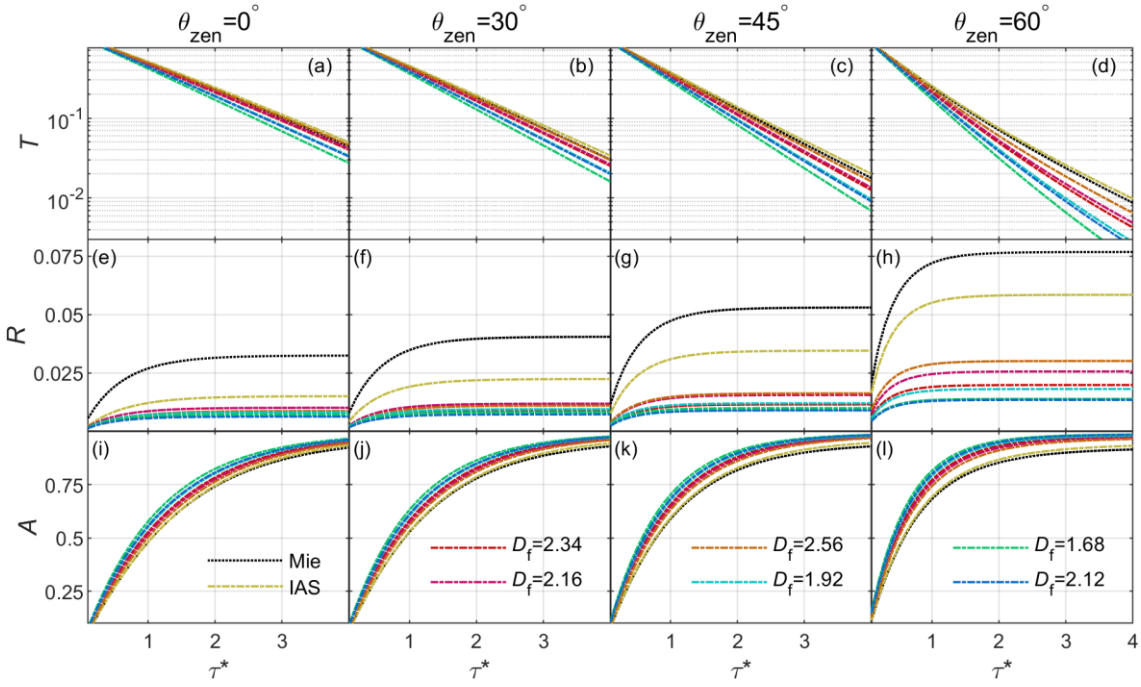

Figure 3. Transmittance, reflectance and absorptance of an atmospheric layer with different BC scatterer shapes as a function of the optical thickness of the layer for different incident zenith angles.

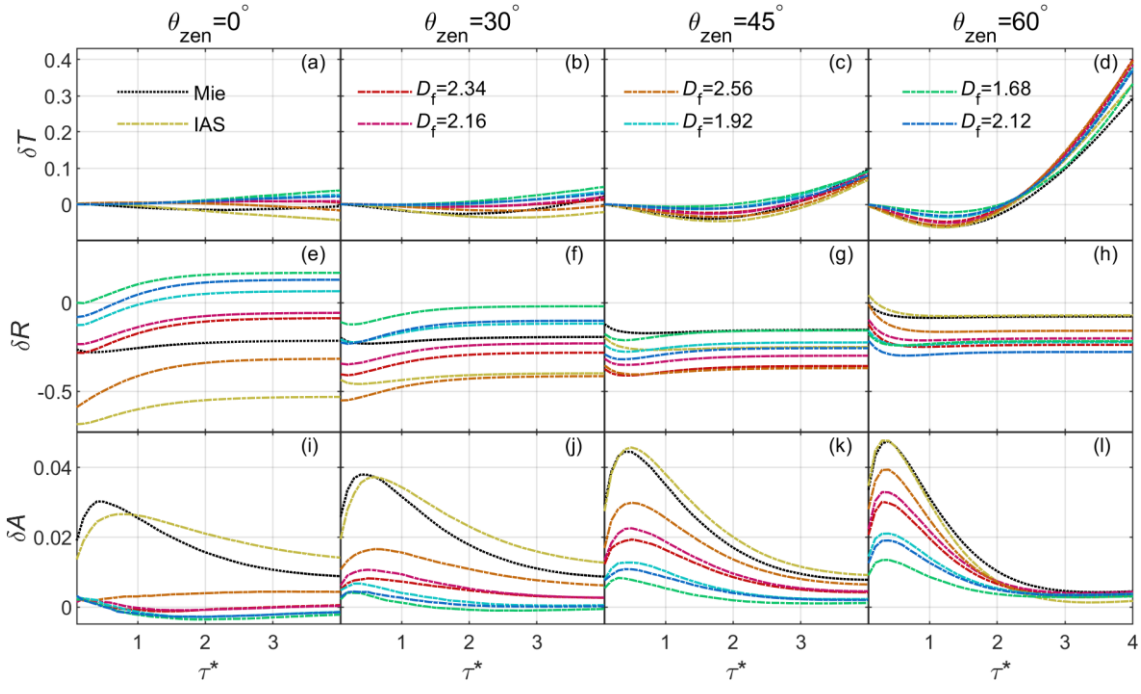

Figure 4. Relative difference in transmittance, reflectance, and absorptance between our MC simulations and the delta-Eddington approximation with different BC scatterer shapes as a function of the optical thickness of the layer for different incident zenith angles.

https://doi.org/10.5194/egusphere-2026-1619
Preprint. Discussion started: 6 May 2026

3.2 The spatial distribution of the intensity and polarization of forward scattered light

In this section, we present the spatial distribution of the intensity and polarization of scattered light that propagates through an atmospheric layer embedded with different types of BC scatterers. The results are for a layer with a total optical thickness of one, and the zenith angles of the incident light are 0° and 30°. To simplify the presentation of the results in this section (and in Sect. 3.3), we have chosen to display three out of six fractal aggregates, along with the IAS aggregate and the Mie sphere. The selection of the fractal aggregate includes the most compact one ($D_f = 2.56$, $k_f = 1.19$), the most extended one ($D_f = 1.68$, $k_f = 1.70$), and one that is neither very compact nor very extended ($D_f = 2.34$, $k_f = 1.08$), all of which were examined in a single scattering sense in Haspel et al. (2023), and the last of which was also examined in a single scattering sense in our recent work (Hefets and Haspel, 2025).

The spatial distribution of the intensity of light scattered through the layer for incident light that is LP, CP, or unpolarized is shown in Figs. 5 and 6 for incident zenith angles of 0° and 30°, respectively. For $\theta_{zen} = 0°$, the direction of propagation of the incident light is directly into the plane of the figure, and for $\theta_{zen} = 30°$, the direction of propagation of the incident light is into the plane of the figure and slightly to the right (along the dashed line marking the incident zenith angle in Fig. 2a), i.e., the head of the scattered beam is on right side of the horizontal axis, and the tail of the scattered beam is on the left side of the horizontal axis. Actually, the distribution of forward scattered intensity for incident CP and for incident unpolarized light are indistinguishable from one another, and thus, they are shown together as one row in Figs. 5 and 6, respectively. From Figs. 5 and 6, we can see that for both incident zenith angles, the area of forward scattered illumination is larger for the Mie sphere and the IAS aggregate than for the fractal aggregates and is slightly larger for the compact fractal aggregate than for the extended fractal aggregates. Additionally, the area of forward scattered illumination with incident LP is more oval than circular and is narrower and more extended along the axis perpendicular to the incident polarization. For $\theta_{zen} = 30°$, for the fractal aggregates, and in particular for the more extended aggregate, the oval symmetry of the scattered area is broken, and the area of forward scattered illumination exhibits symmetry only around the horizontal axis.

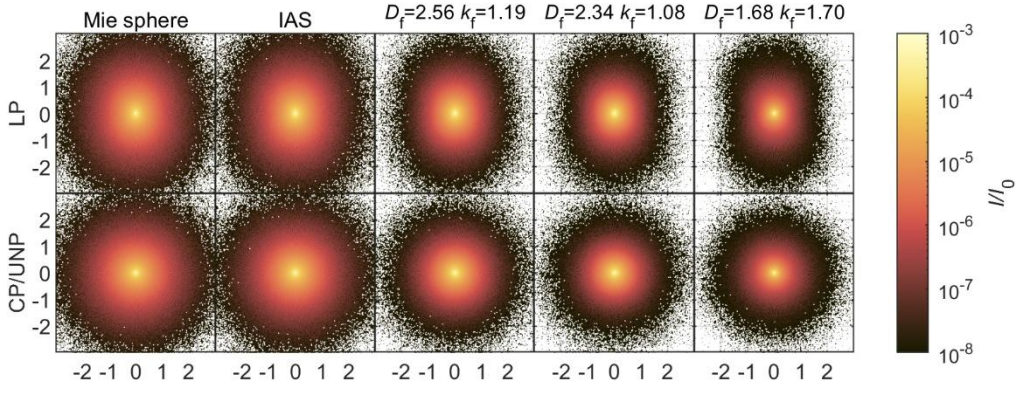

https://doi.org/10.5194/egusphere-2026-1619
Preprint. Discussion started: 6 May 2026

Figure 5. Horizontal (x-y) map of intensity of light forward scattered (transmitted) through an atmospheric layer embedded with different BC scatterer shapes with optical thickness (in the z-direction) of $\tau^* = 1$ and incident zenith angle $\theta_{\text{zen}} = 0°$. The tick labels on the x- and y- axes are in units of optical depth. The intensity distributions for the CP and unpolarized light are indistinguishable from one another and are shown together in the bottom row.

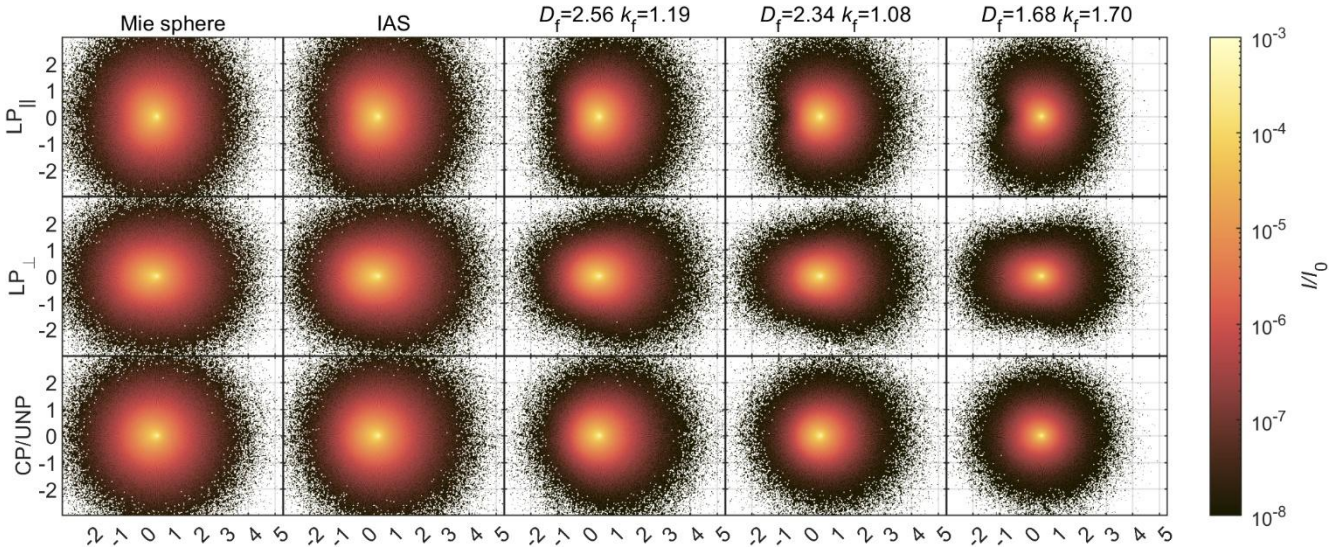

Figure 6. Horizontal (x-y) map of intensity of light forward scattered (transmitted) through an atmospheric layer embedded with different BC scatterer shapes with optical thickness (in the z-direction) of $\tau^* = 1$ and incident zenith angle $\theta_{\text{zen}} = 30°$. The tick labels on the x- and y-axes are in units of optical depth. The intensity distributions for the CP and unpolarized light are indistinguishable from one another and are shown together in the bottom row.

3.2.1 The DoLP of forward scattered light

The spatial distribution of the DoLP of the forward scattered light with an incident zenith angle of 0° is shown in Fig. 7. From Fig. 7, we see that for all of the BC particle shapes and incident LP, the DoLP is relatively high (> 0.8) at the center of the beam. However, in the periphery of the beam, mainly in the horizontal directions above and below the horizontal axis, the DoLP is lower, with a higher gradient of DoLP from the center outward toward the periphery for the Mie sphere, IAS aggregate, and compact fractal aggregate than for the extended fractal aggregate. For incident CP, the center of the beam exhibits very low DoLP (< 0.1), but the periphery of the beam exhibits high DoLP, reaching values of > 0.6 for the Mie sphere and the IAS aggregate and > 0.9 for the extended fractal aggregate. Interestingly, for the fractal aggregates, the DoLP distribution for incident CP is almost identical to the DoLP distribution for incident unpolarized light. For the Mie sphere and the IAS aggregate, however, the DoLP in the peripheral region of the beam is much more substantial for incident CP than for incident unpolarized light.

https://doi.org/10.5194/egusphere-2026-1619
Preprint. Discussion started: 6 May 2026

The spatial distribution of the DoLP of the forward scattered light with an incident zenith angle of 30° is shown in Fig. 8. Like the case of $\theta_{\mathrm{zen}} = 0°$, in the case of $\theta_{\mathrm{zen}} = 30°$ with incident LP, there are areas of low DoLP, and the values of DoLP are lower for the Mie sphere and the IAS aggregate than for the fractal aggregates. Unlike the case of $\theta_{\mathrm{zen}} = 0°$, in the case of $\theta_{\mathrm{zen}} = 30°$ with incident LP, the areas with low DoLP are mainly on the tail side of the beam and tend to be closer to the propagation axis (the horizontal axis) with incident parallel polarization than with incident perpendicular polarization. For incident CP, the central area of low DoLP is now stretched rightward in the direction of propagation of the beam, while the area of high DoLP is now at the tail side of the beam, and the values of DoLP are higher for the more extended fractal aggregate. Like the case of $\theta_{\mathrm{zen}} = 0°$, for the fractal aggregates, the DoLP distribution for incident CP is almost identical to the DoLP distribution for incident unpolarized light, but for the Mie sphere and the IAS aggregate, the DoLP in the peripheral region of the beam is much more substantial for incident CP than for incident unpolarized light.

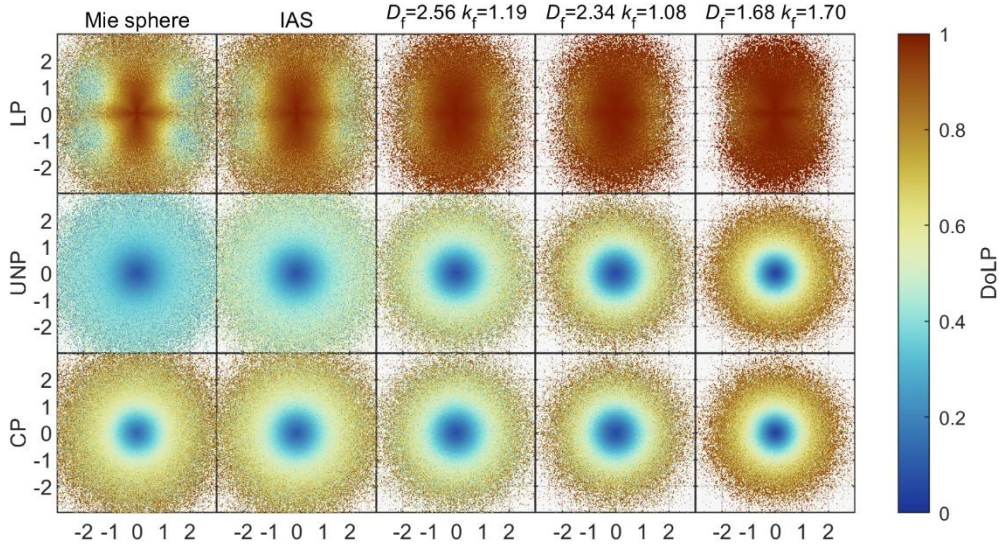

Figure 7. Horizontal (x-y) map of DoLP of light forward scattered (transmitted) through an atmospheric layer embedded with different BC scatterer shapes with optical thickness (in the z-direction) of $\tau^* = 1$ and incident zenith angle $\theta_{\mathrm{zen}} = 0°$. The tick labels on the x- and y-axes are in units of optical depth.

https://doi.org/10.5194/egusphere-2026-1619
Preprint. Discussion started: 6 May 2026

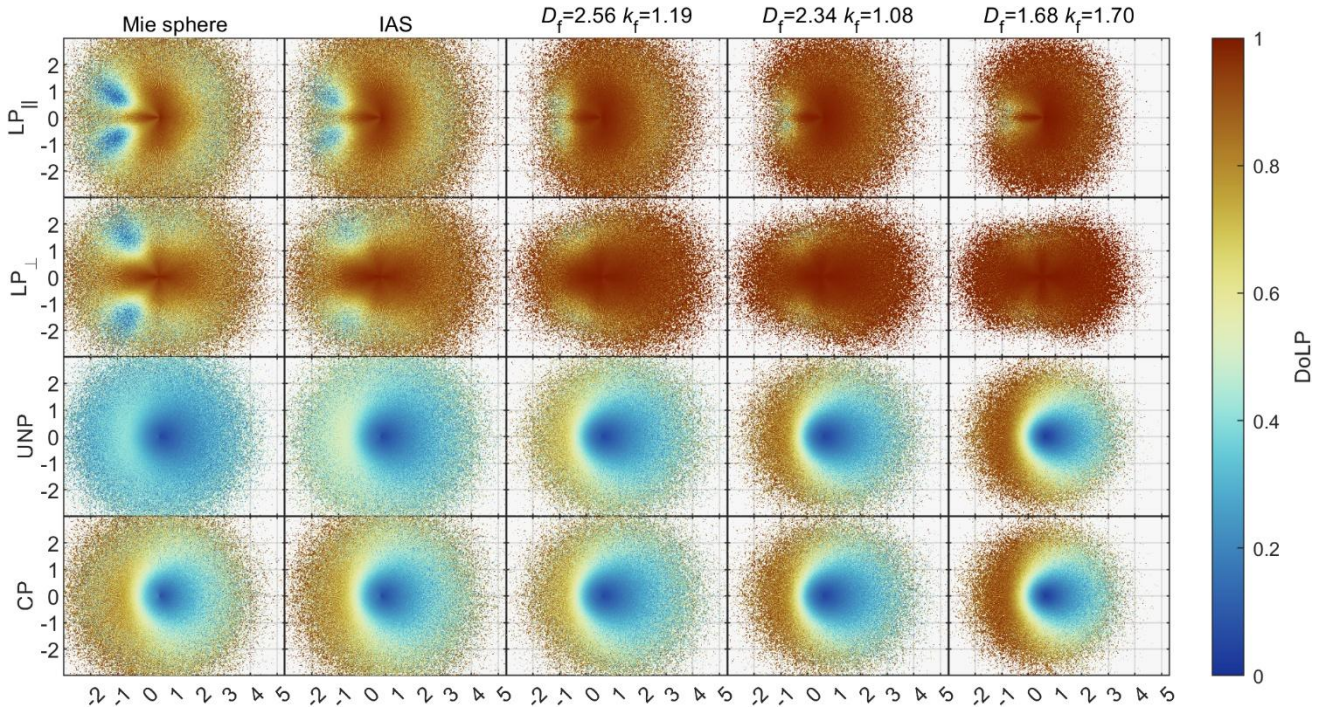

315 Figure 8. Horizontal (x-y) map of DoLP of light forward scattered (transmitted) through an atmospheric layer embedded with different BC scatterer shapes with optical thickness (in the z-direction) of $\tau^* = 1$ and incident zenith angle $\theta_{\text{zen}} = 30°$. The tick labels on the x- and y-axes are in units of optical depth.

3.2.2 The AoLP of forward scattered light

With incident unpolarized light, for all BC particle shapes, the AoLP is always perpendicular to the direction of scattering, i.e., 320 if the direction of scattering is horizontal, then the direction of polarization is vertical, and vice versa. Thus, we do not present AoLP maps for incident unpolarized light here. The spatial distribution of the AoLP of the forward scattered light for incident light that is LP or CP is shown in Figs. 9 and 10 for incident zenith angles of 0° and 30°, respectively. Horizontal polarization is indicated with bright grayish colors, and vertical polarization is indicated with dark colors. With incident LP and zenith angle of 0°, there is almost no difference in AoLP among the different BC particle shapes; the AoLP is parallel to the incident 325 polarization, i.e. $Q \simeq 1$, in both horizontal and vertical scattering directions, and the polarization is slightly diagonal with angle of $\sim \pm 25°$ in transverse scattering directions. With incident CP, as was seen with respect to single scattering in Hefets and Haspel (2025), there is an interesting shift in the AoLP from one BC particle shape to the next: for the most extended aggregate, the AoLP is perpendicular to the direction of scattering direction (the same as with incident unpolarized light), but as the BC particle shape becomes more compact and spherical, the AoLP shifts clockwise and reaches up to ~25° relative to 330 that of the extended fractal aggregate.

https://doi.org/10.5194/egusphere-2026-1619
Preprint. Discussion started: 6 May 2026

For $\theta_{\mathrm{zen}} = 30°$ and incident parallel LP, the AoLP differs among the BC particle shapes mainly on the tail side of the beam, where the region of parallel polarization is wider for the Mie sphere and the IAS aggregate. For $\theta_{\mathrm{zen}} = 30°$ and incident perpendicular LP, the AoLP patterns are similar among the BC particle shapes, but the vertical branches of the exact perpendicular polarization shift toward the tail of the beam in the case of the Mie sphere and the IAS aggregate. As was seen for $\theta_{\mathrm{zen}} = 0°$ and incident CP, for $\theta_{\mathrm{zen}} = 30°$ and incident CP, the AoLP shifts clockwise as the BC particle shape becomes more compact and spherical, and in addition, the shift in the AoLP increases in the upper periphery of the beam.

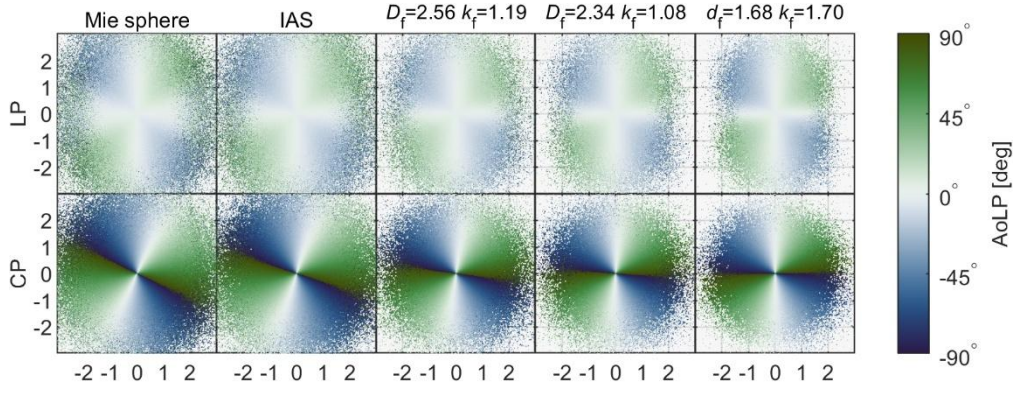

Figure 9. Horizontal (x-y) map of AoLP of light forward scattered (transmitted) through an atmospheric layer embedded with different BC scatterer shapes with optical thickness (in the z-direction) of $\tau^* = 1$ and incident zenith angle $\theta_{\mathrm{zen}} = 0°$. The tick labels on the x- and y-axes are in units of optical depth.

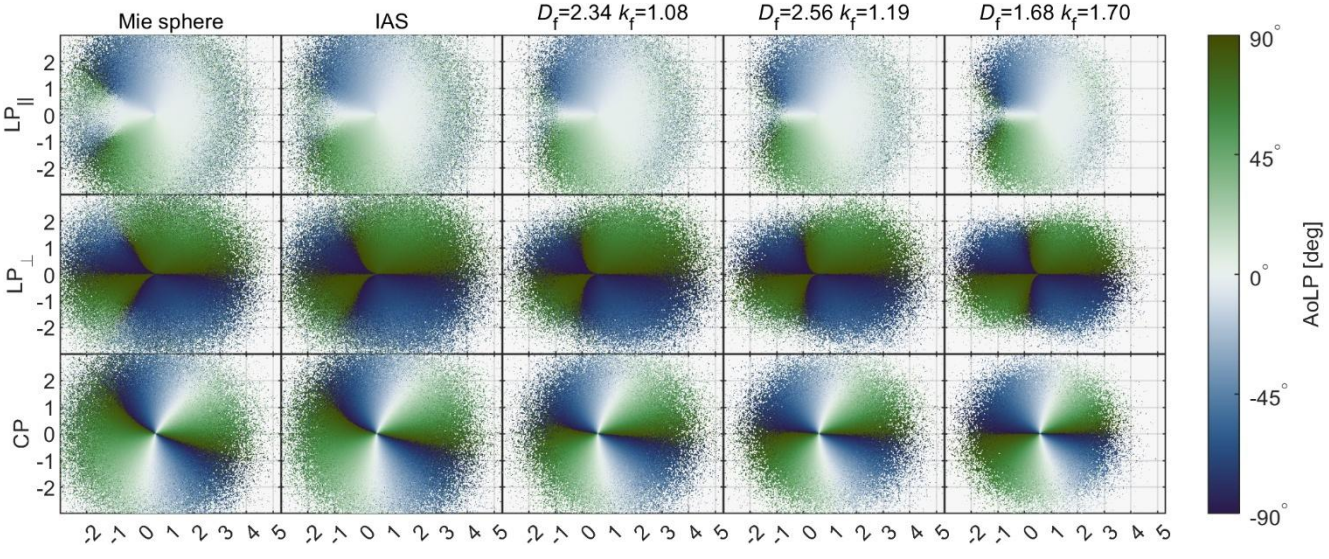

Figure 10. Horizontal (x-y) map of AoLP of light forward scattered (transmitted) through an atmospheric layer embedded with different BC scatterer shapes with optical thickness (in the z-direction) of $\tau^* = 1$ and incident zenith angle $\theta_{\mathrm{zen}} = 30°$. The tick labels on the x- and y-axes are in units of optical depth.

https://doi.org/10.5194/egusphere-2026-1619
Preprint. Discussion started: 6 May 2026

3.2.3 The DoCP of forward scattered light

The spatial distribution of the DoCP of the forward scattered light for incident light that is LP or CP is shown in Figs. 11 and 12 for incident zenith angles of 0° and 30°, respectively. (The DoCP for incident unpolarized light is negligible and thus not shown here.) From Fig. 11, we see that for $\theta_{\mathrm{zen}} = 0°$ and incident parallel LP, there is a nonzero DoCP, but not in the horizontal or vertical scattering directions, which are parallel and perpendicular to the incident polarization, respectively. The DoCP is higher for the Mie sphere and the IAS aggregate than for the fractal aggregates. For $\theta_{\mathrm{zen}} = 0°$ and incident CP, there is a very high DoCP in the center of the beam and a lower DoCP in the periphery of the beam for all BC particle shapes. Interestingly, in this case, the DoCP in the periphery of the beam is higher for the IAS aggregate and the more compact fractal aggregates but lower for the Mie sphere and for the most extended fractal aggregate. From Fig. 12, we see that for $\theta_{\mathrm{zen}} = 30°$ and incident LP, the DoCP is nonzero mostly for the Mie sphere and the IAS aggregate and mainly on the tail side of the beam, reaching a value of ~0.6. For $\theta_{\mathrm{zen}} = 30°$ and incident CP, the tendency is the opposite; the DoCP is higher for the fractal aggregates and is higher from the center to the head side of the beam.

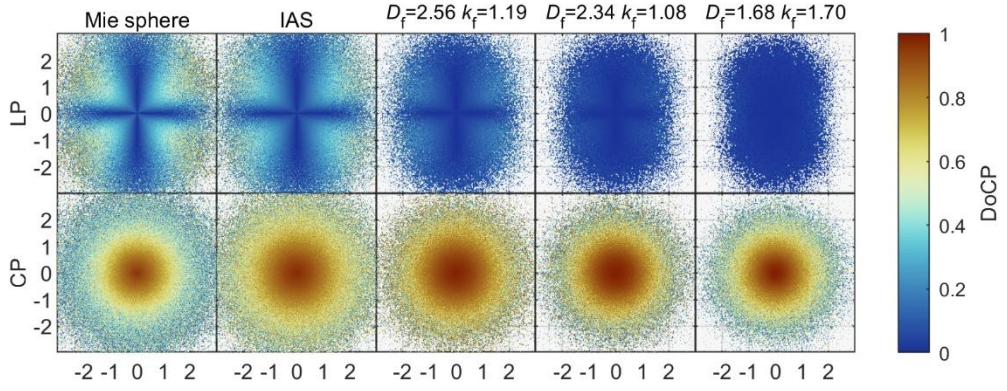

Figure 11. Horizontal (x-y) map of DoCP of light forward scattered (transmitted) through an atmospheric layer embedded with different BC scatterer shapes with optical thickness (in the z-direction) of $\tau^* = 1$ and incident zenith angle $\theta_{\mathrm{zen}} = 0°$. The tick labels on the x- and y-axes are in units of optical depth.

https://doi.org/10.5194/egusphere-2026-1619
Preprint. Discussion started: 6 May 2026

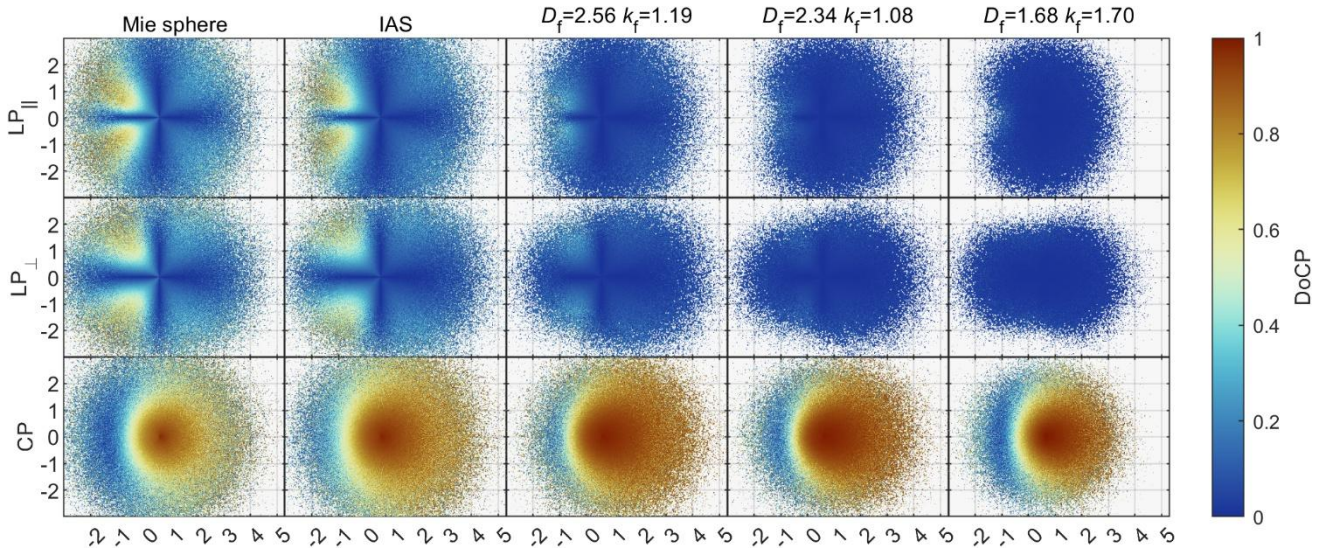

Figure 12. Horizontal (x-y) map of DoCP of light forward scattered (transmitted) through an atmospheric layer embedded with different BC scatterer shapes with optical thickness (in the z-direction) of $\tau^* = 1$ and incident zenith angle $\theta_{\text{zen}} = 30°$. The tick labels on the x- and y-axes are in units of optical depth.

3.3 The spatial distribution of the intensity and polarization of backscattered light

In this section, we present the spatial distribution of the intensity and polarization of scattered light that is scattered back from an atmospheric layer embedded with different types of BC scatterers, i.e., in a similar fashion to Sect. 3.2 but for backscattered light rather than for forward scattered light. Once again, the results are for a layer with a total optical thickness of one, and the zenith angles of the incident light are 0° and 30°, and we display results for the same list of BC particle shapes: the Mie sphere, the IAS aggregate, the most compact fractal aggregate ($D_f = 2.56$, $k_f = 1.19$), a fractal aggregate that is neither very compact nor very extended ($D_f = 2.34$, $k_f = 1.08$), and the most extended fractal aggregate ($D_f = 1.68$, $k_f = 1.70$).

The spatial distribution of the intensity of light scattered back from the layer for incident light that is LP, CP, or unpolarized is shown in Figs. 13 and 14 for incident zenith angles of 0° and 30°, respectively. In Figs. 13 and 14, as well as in the remaining figures in this section, the incident light propagates into the plane of the figure, and the reflected light is scattered backward from the plane (refer to Fig. 2a). As with the forward scattered intensity, the spatial distribution of the backscattered intensity for incident CP and for incident unpolarized light are indistinguishable from one another, and thus, they are shown together as one row in Figs. 13 and 14, respectively. From Figs. 13 and 14, we can see that as opposed to the distribution of forward scattered intensity, the distribution of backward scattered intensity for the compact fractal aggregate is more similar to that of the other fractal aggregates than to that of the Mie sphere and the IAS aggregate. Like the forward scattered intensity, for incident LP and for both incident zenith angles, the area of backscattered illumination is narrower and more extended along

https://doi.org/10.5194/egusphere-2026-1619
Preprint. Discussion started: 6 May 2026

the axis perpendicular to the incident polarization, but the area is narrower along the horizontal axis than the area of forward scattered illumination, and for incident parallel LP and $\theta_{\mathrm{zen}} = 30°$, the break in vertical symmetry is in the opposite direction to the break in vertical symmetry of the area of forward scattered illumination (refer to Fig. 6).

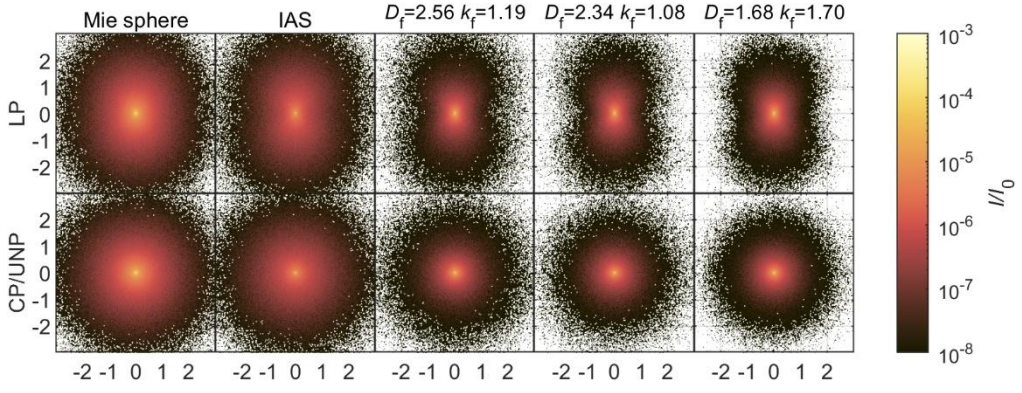

385 Figure 13. Horizontal (x-y) map of intensity of light backscattered (reflected) from an atmospheric layer embedded with different BC scatterer shapes with optical thickness (in the z-direction) of $\tau^* = 1$ and incident zenith angle $\theta_{\mathrm{zen}} = 0°$. The tick labels on the x- and y-axes are in units of optical depth. The intensity distributions for the CP and unpolarized light are indistinguishable from one another and are shown together in the bottom row.

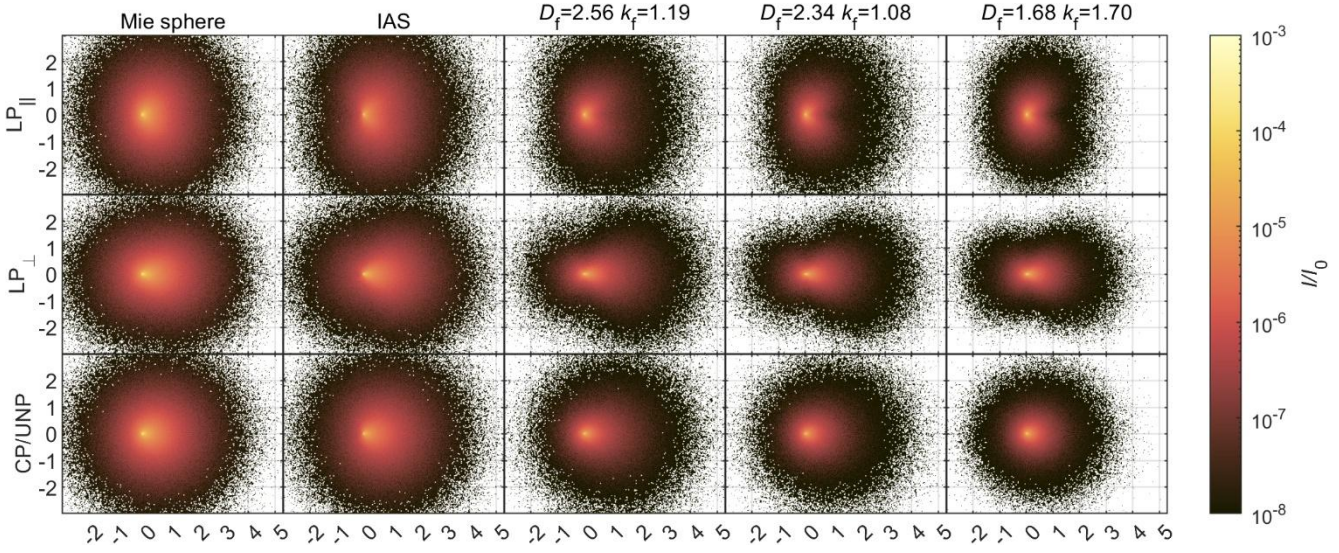

390 Figure 14. Horizontal (x-y) map of intensity of light backscattered (reflected) from an atmospheric layer embedded with different BC scatterer shapes with optical thickness (in the z-direction) of $\tau^* = 1$ and incident zenith angle $\theta_{\mathrm{zen}} = 30°$. The tick labels on the x- and y-axes are in units of optical depth. The intensity distributions for the CP and unpolarized light are indistinguishable from one another and are shown together in the bottom row.

3.3.1 The DoLP of backscattered light

https://doi.org/10.5194/egusphere-2026-1619
Preprint. Discussion started: 6 May 2026

The spatial distribution of the DoLP of the backscattered light with an incident zenith angle of 0° and with an incident zenith angle of 30° is shown in Fig. 15 and Fig. 16, respectively. From Fig. 15, we see that with $\theta_{\mathrm{zen}} = 0°$ and incident LP, the distribution of the DoLP exhibits an X-like pattern of relatively low DoLP; this low DoLP area is larger in size and lower in value (< 0.2) for the Mie sphere and the IAS aggregate and is smaller size and higher in value (> 0.4) for the fractal aggregates. From Fig. 16, with $\theta_{\mathrm{zen}} = 30°$ and incident LP, the X shape of the low DoLP area becomes asymmetric, with its head side arms having lower DoLP than its tail side arms. However, for both incident zenith angles, the values of the high DoLP areas are larger for the fractal aggregates than for the Mie sphere or the IAS aggregate.

Like for the forward scattered light (Sect. 3.2.1), in the case of the fractal aggregates, for both incident zenith angles, the spatial distribution of the DoLP of the backscattered light with incident CP is almost identical to spatial distribution of the DoLP of the backscattered light with incident unpolarized light, while for the Mie sphere and the IAS aggregate, the spatial distribution of the DoLP of the backscattered light with incident CP is much higher than spatial distribution of the DoLP of the backscattered light with incident unpolarized light. For the fractal aggregates, for both zenith angles, the DoLP is very low (< 0.2) at the center of the beam and is relatively high (> 0.7) at the periphery of the beam. For the Mie sphere and the IAS aggregate, for both incident zenith angles, with incident CP, the DoLP of backscattered light is relatively high ($\lesssim 0.8$ and $\lesssim 0.9$, respectively), and the area of low DoLP at the center of the beam is very small, but with incident unpolarized light, the DoLP of backscattered light is relatively low ($\lesssim 0.4$ and $\lesssim 0.5$, respectively). In addition, for all BC particle shapes and for both incident CP and unpolarized light, for $\theta_{\mathrm{zen}} = 30°$, the low DoLP area shifts from the center to the tail side of the beam.

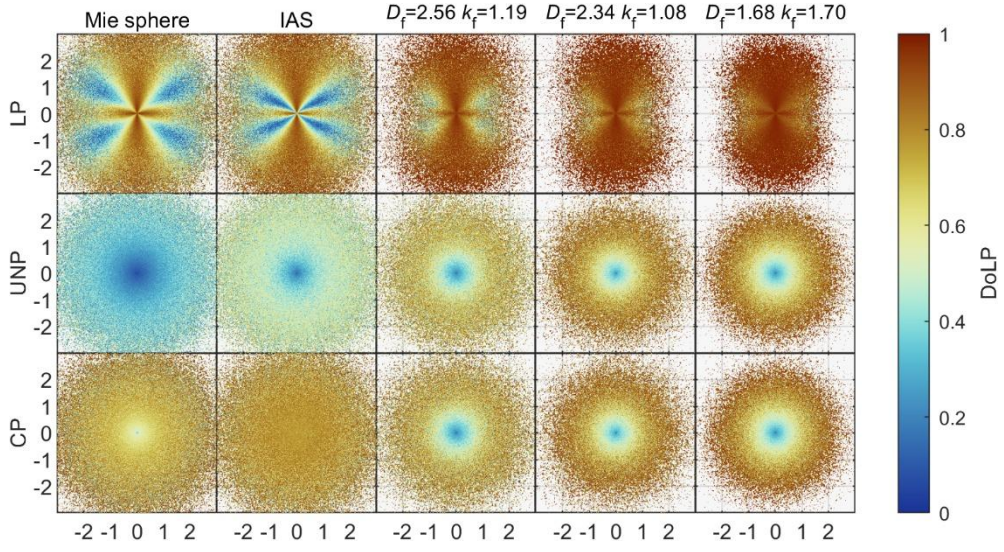

Figure 15. Horizontal (x-y) map of DoLP of light backscattered (reflected) from an atmospheric layer embedded with different BC scatterer shapes with optical thickness (in the z-direction) of $\tau^* = 1$ and incident zenith angle $\theta_{\mathrm{zen}} = 0°$. The tick labels on the x- and y-axes are in units of optical depth.

https://doi.org/10.5194/egusphere-2026-1619
Preprint. Discussion started: 6 May 2026

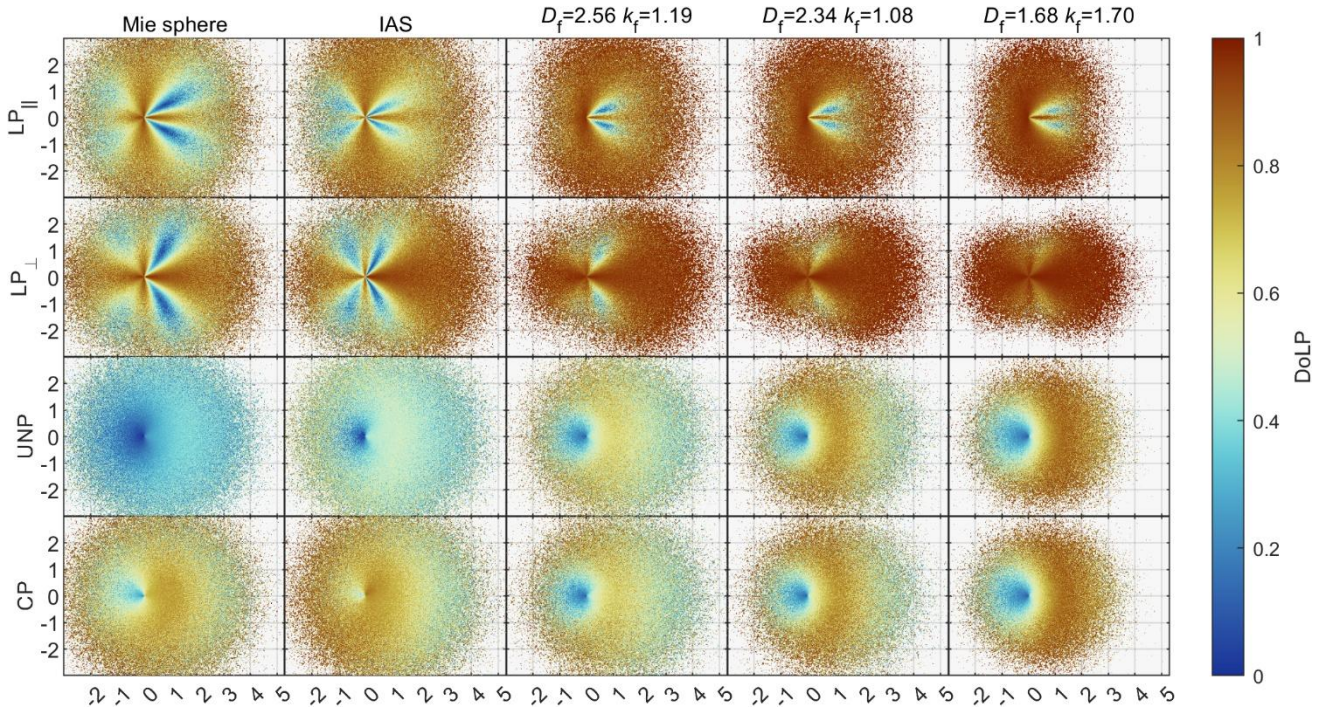

Figure 16. Horizontal (x-y) map of DoLP of light backscattered (reflected) from an atmospheric layer embedded with different BC scatterer shapes with optical thickness (in the z-direction) of $\tau^* = 1$ and incident zenith angle $\theta_{\text{zen}} = 30°$. The tick labels on the x- and y-axes are in units of optical depth.

3.3.2 The AoLP of backscattered light

The spatial distribution of the AoLP of the backscattered light for incident zenith angle 0° is shown in Fig. 17. From Fig. 17, we see that with incident LP, the AoLP of backscattered light of the fractal aggregates is similar to the AoLP of forward scattered light of the fractal aggregates (refer to Sect. 3.2.2), but for the Mie sphere and the IAS aggregate, the tendency of the AoLP of the backscattered light differs from that of the forward scattered light. For the Mie sphere and the IAS aggregate, the orientation of the diagonal polarization in the transverse scattering direction changes within the same quadrant, and for the IAS aggregate, the AoLP even becomes perpendicular ($Q = -1$) in the backscattering angle range of $\sim 25° - 30°$ relative to the horizontal axes.

The spatial distribution of the AoLP of the backscattered light for incident zenith angle 30° is shown in Fig. 18. From Fig. 18, we see that with incident parallel LP, for all of the BC particle shapes, the orientation of the diagonal polarization in the transverse scattering direction changes within the same quadrant, on the head side of the beam. With incident perpendicular LP, as opposed to the case of forward scattered light, in which all of the vertical branches of the exact perpendicular polarization (AoLP equal to 90°) tend toward the tail of the beam (refer to Fig. 10), in the case of backscattered light, the vertical branches

https://doi.org/10.5194/egusphere-2026-1619
Preprint. Discussion started: 6 May 2026

with full perpendicular polarization tend toward the head of the beam, and for the Mie sphere, the IAS aggregate, and the more compact fractal aggregate, those vertical branches are partially fully polarized parallel to the horizontal axis (AoLP equal to 0°). In addition, for both incident zenith angles, as opposed to the case of forward scattered light in which the AoLP shifts clockwise with incident CP (refer to Figs. 9 and 10), in the case of backscattered light, the AoLP shifts counterclockwise with incident CP.

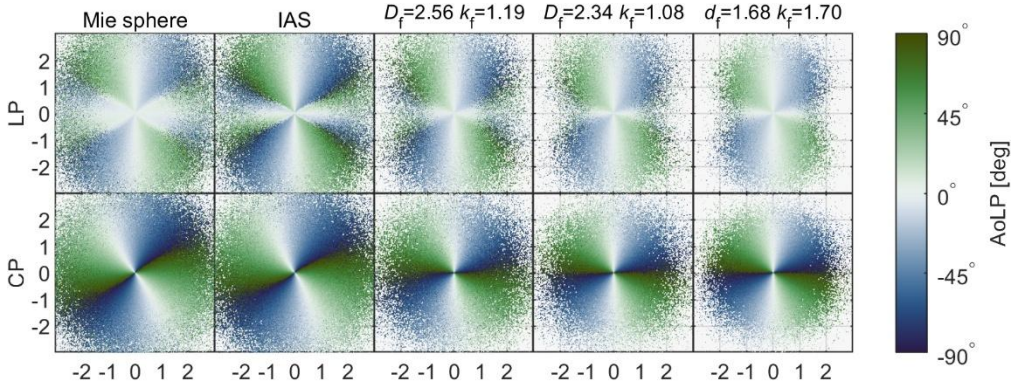

Figure 17. Horizontal (x-y) map of AoLP of light backscattered (reflected) from an atmospheric layer embedded with different BC scatterer shapes with optical thickness (in the z-direction) of $\tau^* = 1$ and incident zenith angle $\theta_{\text{zen}} = 0°$. The tick labels on the x- and y-axes are in units of optical depth.

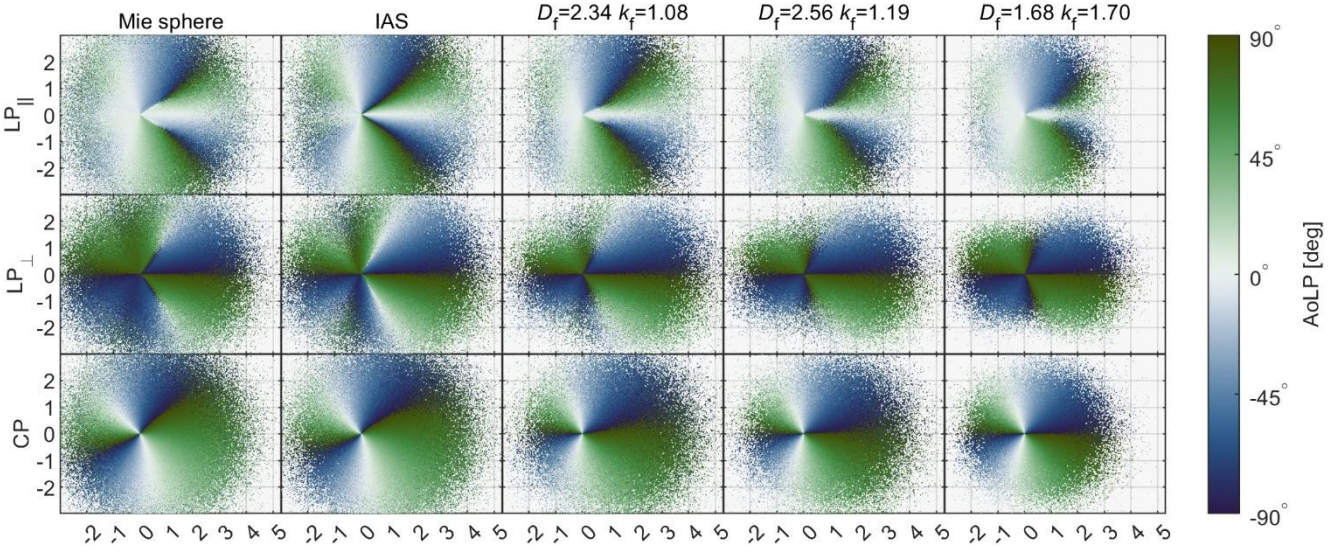

Figure 18. Horizontal (x-y) map of AoLP of light backscattered (reflected) from an atmospheric layer embedded with different BC scatterer shapes with optical thickness (in the z-direction) of $\tau^* = 1$ and incident zenith angle $\theta_{\text{zen}} = 30°$. The tick labels on the x- and y-axes are in units of optical depth.

https://doi.org/10.5194/egusphere-2026-1619
Preprint. Discussion started: 6 May 2026

3.3.3 The DoCP of backscattered light

The spatial distribution of the DoCP of the backscattered light for incident zenith angle 0° is shown in Fig. 19. From Fig. 19, we see that for $\theta_{\mathrm{zen}} = 0°$ and incident parallel LP, for the Mie sphere and the IAS aggregate, there is an X-shaped area of relatively high DoCP in the backscattered light with values > 0.7, while for the fractal aggregate, the DoCP is very low with values < 0.2. With incident CP, for all of the BC particle shapes, the DoCP of the backscattered light is considerably lower than in the case of forward scattered light (refer to Fig. 11), but for the fractal aggregates, the center area of the beam is highly circularly polarized (DoCP> 0.8). Interestingly, for the Mie sphere, the area of high DoCP is much smaller than for the fractal aggregate, and for the IAS aggregate, the DoCP is relatively low (< 0.4) even at the center of the beam. Additionally, for both the IAS aggregate and the compact fractal aggregate, the DoCP in the periphery of the beam increases up to values of ~ 0.5.

The spatial distribution of the DoCP of the backscattered light for incident zenith angle 30° is shown in Fig. 20. From Fig. 20, we see that for $\theta_{\mathrm{zen}} = 30°$ and both incident parallel and perpendicular LP, the DoCP patterns are similar to the DoCP patterns for $\theta_{\mathrm{zen}} = 0°$ (in which for the Mie sphere and the IAS aggregate, the distribution of DoCP exhibits an X-shape), except that for $\theta_{\mathrm{zen}} = 30°$, the X-shape is asymmetric, with higher DoCP higher in the arms of the X on the head side of the beam. For $\theta_{\mathrm{zen}} = 30°$ and incident CP, there are two areas of relatively high DoCP levels in the light backscattered from the fractal aggregates: one area, with DoCP >0.6, is on the head side of the beam, and its size increases with the compactness of the fractal aggregate, and the second area, with DoCP values >0.9 at its center, tends toward the tail side of the beam. Between those two areas, there is an area of very low DoCP (<0.2). For the Mie sphere and the IAS aggregate, and for both incident zenith angles, the patterns of the DoCP distribution are similar to those of the fractal aggregates. However, the area with high DoCP in the center or on the tail side of the beam, respectively, is smaller in size than for the fractal aggregates, and for the IAS aggregate, this area almost vanishes, and the DoCP is lower ($\lesssim 0.5$) there than for the other BC particles. Nevertheless, for $\theta_{\mathrm{sca}} = 30°$, the area with relatively high DoCP on the head side of the beam is larger in area and in absolute value for the IAS aggregate than for the Mie sphere.

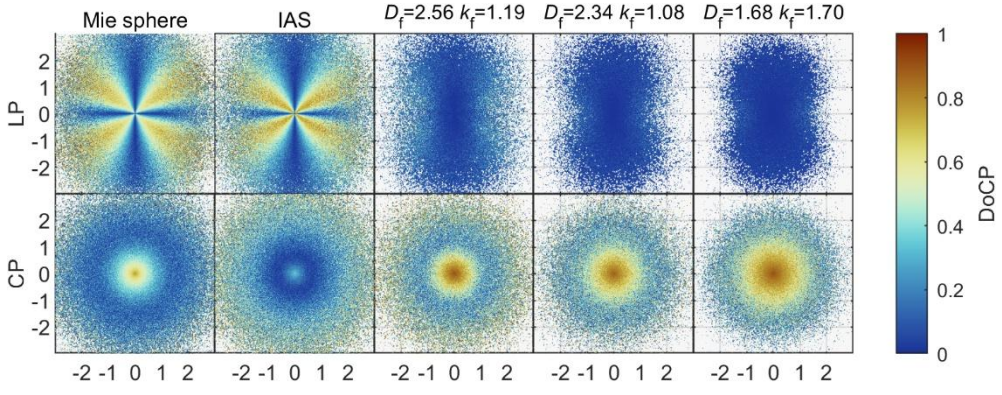

https://doi.org/10.5194/egusphere-2026-1619
Preprint. Discussion started: 6 May 2026

Figure 19. Horizontal (x-y) map of DoCP of light backscattered (reflected) from an atmospheric layer embedded with different BC scatterer shapes with optical thickness (in the z-direction) of $\tau^* = 1$ and incident zenith angle $\theta_{\mathrm{zen}} = 0°$. The tick labels on the x- and y-axes are in units of optical depth.

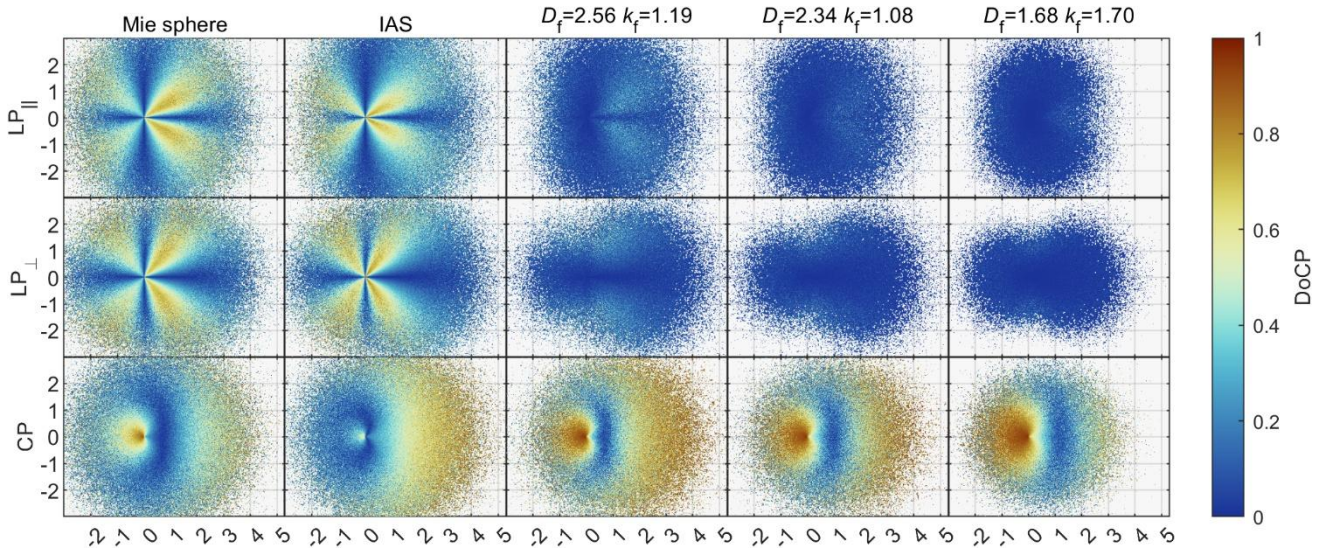

Figure 20. Horizontal (x-y) map of DoCP of light backscattered (reflected) from an atmospheric layer embedded with different BC scatterer shapes with optical thickness (in the z-direction) of $\tau^* = 1$ and incident zenith angle $\theta_{\mathrm{zen}} = 30°$. The tick labels on the x- and y-axes are in units of optical depth.

4 Summary

In this study, we used a specially designed MC model to investigate the multiple scattering of light in an atmospheric layer embedded with BC particles of various shapes, from a perfect Mie sphere to compact aggregates to extended aggregates. Our MC model is unique in that for each individual scattering event, we select the Mueller matrix for that event using selection rules designed to mimic the fact that during each event, the incident light encounters an individual realization of a scatterer shape in its individual orientation.

We found that the transmittance of an atmospheric layer embedded with BC particles is highest when the particles are more spherical, moderate when the particles are compact fractal aggregates, and lowest when the particles are extended fractal aggregates, with an overall difference of approximately 10% relative to the incident intensity between the highest and lowest values of transmittance. Moreover, this difference increases with increasing incident zenith angle. The reflectance exhibits a similar tendency, with the highest reflectance for the more spherical BC particle shapes and the lowest reflectance for the more extended fractal aggregates, with the difference increasing with increasing incident zenith angle. Correspondingly, the layer absorptance is lowest for the more spherical BC shapes and highest for the extended fractal aggregates, again with the

https://doi.org/10.5194/egusphere-2026-1619
Preprint. Discussion started: 6 May 2026

difference increasing with increasing incident zenith angle. The fact that the absorption cross section of BC fractal aggregates is generally higher and thus the single scattering albedo is generally lower for more extended aggregate shapes than for more compact aggregate shapes has been found previously in the context of single scattering (see, e.g., Liu and Mishchenko (2005), Liu et al. (2008), Soewono and Rogak (2013), Romshoo et al. (2021, 2022), Haspel et al. (2023), Hefets and Haspel (2025)). Here we find the same tendency (more absorption for more extended aggregate shapes) in the context of multiple scattering as well. This important result can contribute to efforts to provide better closure between calculations and measurements of absorption by light absorbing carbon in general (see, e.g., Bond and Bergstrom (2006)).

In addition, we compared the BC layer transmittance, reflectance, and absorptance obtained from our MC simulations with those obtained with a conventional radiative transfer approximation (the delta-Eddington approximation) for the same optical thickness, single scattering albedo, and asymmetry factor. We found that there is a relatively small difference between the layer transmittance obtained with our MC simulations and the layer transmittance obtained with the delta-Eddington approximation and a relatively small difference between the layer absorptance obtained with our MC simulations and the layer absorptance obtained with the delta-Eddington approximation. However, the layer *reflectance* obtained with our MC simulations is up to 50% lower than that obtained with the delta-Eddington approximation for the IAS sphere and for the most compact fractal aggregate and up to 15-35% lower than that obtained with the delta-Eddington approximation for the other BC particle shapes. Taken together with the finding stated above that in single and multiple scattering, more extended BC fractal aggregates tend to lead to higher layer absorptance than more spherical shaped BC particles, our results regarding the absorptance and reflectance of atmospheric layers containing BC could have important implications for radiative forcing estimations and climate modeling.

Regarding the spatial distribution of the scattered intensity, we found that for all incident polarizations (LP, CP, and unpolarized), for both transmitted and reflected light, the area of scattered illumination is broader for more spherical BC particle shapes than for fractal BC aggregates. This difference occurs for both incident zenith angles of 0° and 30° and is more prominent in the case of incident LP, when the area of scattered illumination is oval shaped. There are also small but distinguishable differences among the scattering patterns of reflected light of the various fractal aggregates for $\theta_{\mathrm{zen}} = 30°$.

We found that the spatial distribution of the DoLP and the spatial distribution of the DoCP are also sensitive to BC particle shape, though the differences among the shapes are more prominent for reflected light, especially at large incident zenith angles, than for transmitted light and are more prominent for incident LP than for incident CP. We found that BC particles cause fairly strong depolarization of incident LP (DoLP values < 0.5), with the depolarization occupying broader areas of the scattered light distribution for more spherical BC shapes than for fractal BC aggregates. As with the stronger absorption by more extended BC particle shapes, the stronger depolarization of LP by more spherical shapes than by more extended aggregate shapes has also been found previously in the context of single scattering (see, e.g., Kahnert and Kanngießer (2020) and Hefets

https://doi.org/10.5194/egusphere-2026-1619
Preprint. Discussion started: 6 May 2026

and Haspel (2025)), and here we find the same tendency in multiple scattering as well. Similarly, we found that there is also fairly strong depolarization of incident CP (DoCP values < 0.5) for all BC particle shapes, with the depolarization of circularly polarized incident light more prominent for reflected light than for transmitted light and prominent in the transmitted light mostly for $\theta_{\mathrm{zen}} = 30°$. We found that interestingly, for the more spherical BC shapes, the DoLP is much higher for incident CP than for incident unpolarized light, but for fractal aggregates, the DoLP is nearly identical for incident CP and incident unpolarized light. Also interestingly, we found that for the more spherical BC shapes and incident LP, there is a fairly strong creation of circular polarization (DoCP values > 0.5) in broad areas of the illuminated beam for both transmitted and reflected light, with larger areas of DoCP created for reflected light. Once again, this phenomenon (the increasing of the DoCP by scattering by BC particles with incident LP and its greater prominence for more compact, more spherical BC particles) has been found previously in the context of single scattering (see, e.g., Liu and Mishchenko (2005, 2007)), and here we find the same tendency in multiple scattering as well. Additionally, we found that for incident CP, the AoLP shifts clockwise for transmitted light and counterclockwise for reflected light, and the shift is larger the more compact and spherical and the less extended the BC particle shape.

Based on the above, we suggest that in addition to analysis of scattered intensity, the sensitivity of the scattered DoLP and DoCP and to a lesser extent the scattered AoLP to BC particle shape could be useful for retrieving information on BC particle morphology via remote sensing and/or in situ field measurements of aerosol particle scattering, and further examination of this possibility should be explored in future investigations.

Appendix A: Difference in the scattering angle distribution between our individual Mueller matrix selection method and the conventional pre-averaged Mueller matrix method

As mentioned in Sect. 2.2, in our simulations, we used an individual Mueller matrix for each scattering event. Here, we demonstrate the difference between our approach and the conventional method of using the pre-averaged Mueller matrix. We simulate 10^7 events of single scattering of LP photons from one of the realizations of the most extended fractal aggregate ($D_{\mathrm{f}} = 1.68$, $k_{\mathrm{f}} = 1.70$), and we map the distribution of photons as a function of scattering direction (θ_{sca}, ϕ_{sca}). We repeat the simulation 10 times using the conventional pre-averaged Mueller matrix method and another 10 times using our individual Mueller matrix selection method.

To illustrate the anisotropy of scattering from different orientations, in Fig. A1, we present two arbitrary orientations of the fractal aggregate. In the simulation, the incident photons propagate along the z axis, and the polarization is parallel to the x

https://doi.org/10.5194/egusphere-2026-1619
Preprint. Discussion started: 6 May 2026

axis. The scattering phase functions for each of the two orientations of the fractal aggregate from Fig. A1 and the scattering phase function for the same aggregate obtained from the pre-averaged Mueller matrix are shown in Fig. A2.

The photon count as a function of scattering direction, $N(\theta_{sca}, \phi_{sca})$, averaged over the 10 repetitions conducted using the conventional pre-averaged Mueller matrix method is shown in Fig. A3a. The difference in photon count between the two methods, ΔN, is shown in Fig. A3b, and the relative difference in photon count, δN, with the relative difference defined as in Eq. 13, is shown in Fig. A3c. Positive values in Figs. A3b and A3c indicate a higher photon count in our individual Mueller matrix selection method than for the conventional pre-averaged Mueller matrix method, and vice versa. We can see that the relative difference is strongest in directions perpendicular to the incident polarization ($\phi_{sca} = 90°, 270°$). In forward scattering directions ($\theta_{sca} \simeq 10° - 30°$), the relative difference is negative with absolute values between ~0.03 and ~0.05, and in backscattering directions ($100° < \theta_{sca} < 160°$), the relative difference is positive with values between 0.01 and 0.1.

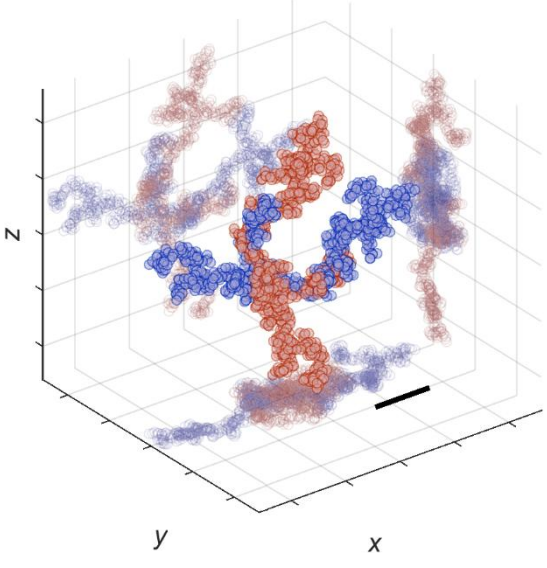

Figure A1. Two arbitrary orientations (indicated with blue and red colors, respectively) of the most extended fractal aggregate ($D_f = 1.68$, $k_f = 1.70$) and their projections. The grid spacing and the length of the scale bar are each 0.5 μm.

https://doi.org/10.5194/egusphere-2026-1619
Preprint. Discussion started: 6 May 2026

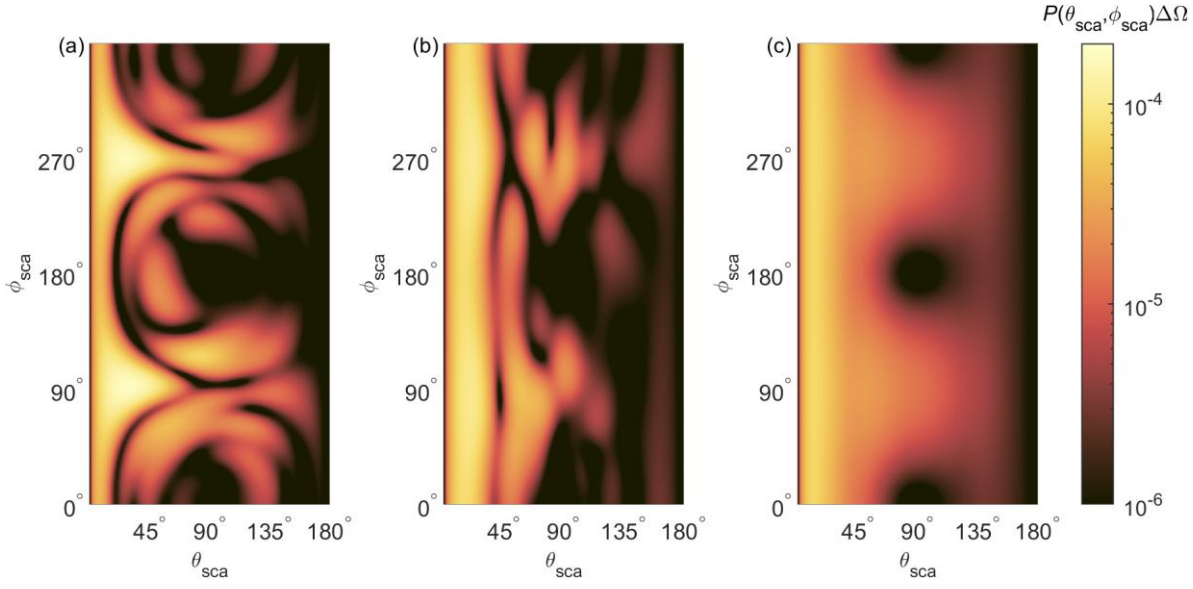

Figure A2. The single scattering phase function, $P(\theta_{sca}, \phi_{sca})$ multiplied by the interval of solid angle ($\Delta\Omega$) for the most extended aggregate (a) oriented in the 'blue' orientation from Fig. A1, (b) oriented in the 'red' orientation from Fig. A1, and (c) averaged over all orientations. The incident light is LP.

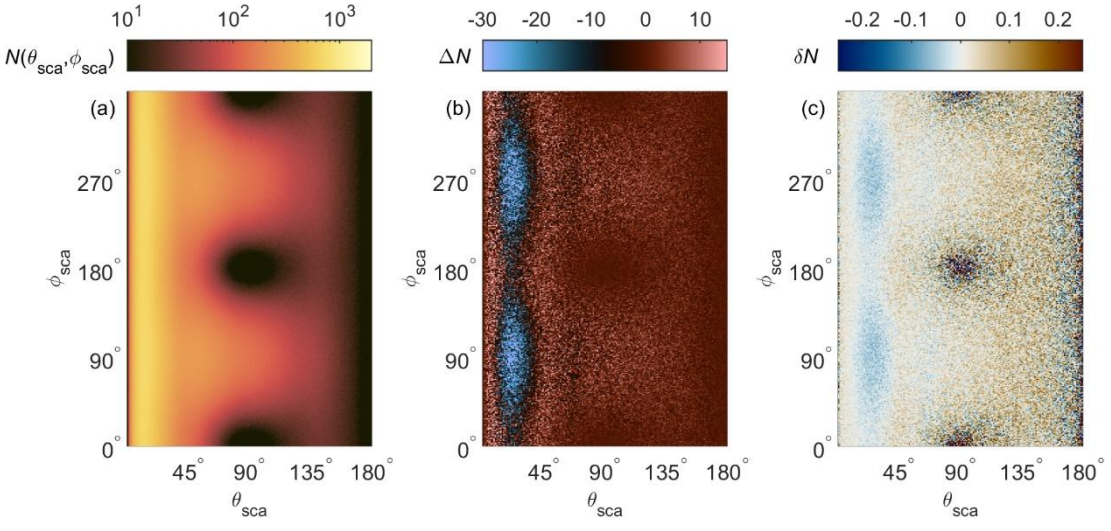

Figure A3. (a) Photon count as a function of scattering direction, $N(\theta_{sca}, \phi_{sca})$, averaged over the 10 repetitions conducted using the conventional pre-averaged Mueller matrix method (b) difference in photon count, ΔN, between our individual Mueller matrix selection method than for the conventional pre-averaged Mueller matrix method; (c) relative difference in photon count, δN, between our individual Mueller matrix selection method than for the conventional pre-averaged Mueller matrix method.

https://doi.org/10.5194/egusphere-2026-1619
Preprint. Discussion started: 6 May 2026

Code and data availability. The single scattering MATLAB code is available at https://doi.org/10.5281/zenodo.18995083 (Hefets and Haspel, 2026a), the Monte Carlo multiple scattering MATLAB code is available at https://doi.org/10.5281/zenodo.19043053 (Hefets and Haspel, 2026b), and the input data of the BC particles is available at https://doi.org/10.5281/zenodo.19041638 (Haspel and Hefets, 2026).

Author contribution. YH performed the simulations and the data analysis under the supervision of CH; both authors prepared the manuscript.

Competing interests. The contact author has declared that none of the authors has any competing interests.

Acknowledgements. We thank Emanuel Boss for providing us with the Mie scattering code in MATLAB, Zbigniew H. Stachurski for providing us with the IAS generating algorithm, and Daniel Mackowski for providing us with the fractal aggregate generating algorithm.

Financial support. This work was funded by the Israel Science Foundation Grant 2187/21.

References

Bartel, S. and Hielscher, A. I.: Monte Carlo simulations of the diffuse backscattering Mueller matrix for highly scattering media, Appl. Opt., 39, 1580-1588, 2000.

Bohren, C. F. and Huffman, D. R.: Absorption and Scattering of Light by Small Particles, Wiley-VCH, Germany, ISBN 978-3-527-61816-3, 1983.

Bond, T. C. and Bergstrom, R. W.: Light absorption by carbonaceous particles: An investigative review, Aerosol Sci. Tech., 40, 27–67, https://doi.org/10.1080/02786820500421521, 2006

Bond, T. C., Habib, G, and Bergstrom, R. W.: Limitations in the enhancement of visible light absorption due to mixing state, J. Geophys. Res.-Atmos., 111, D20211, https://doi.org/10.1029/2006JD007315, 2006.

Boss, E.: Adaptation of a Fortran Code of Bohren & Huffman to MATLAB, University of MAINE, 1998.

Briegleb, B.P.: Delta-Eddington approximation for solar radiation in the NCAR community climate model, J. Geophys. Res.-Atmos., 97(D7), 7603–7612, https://doi.org/10.1029/92JD00291, 1992.

Chaikovskaya, L. I.: Remote sensing of clouds using linearly and circularly polarized laser beams: techniques to compute signal polarization, in: Light Scattering Reviews 3, edited by: Kokhanovsky, A. A., Springer, Berlin, Heidelberg, Germany, 191–228, https://doi.org/10.1007/978-3-540-48546-9_6, 2008

Chami, M., Santer, R, and Dilligeard, E.: Radiative transfer model for the computation of radiance and polarization in an ocean-atmosphere system: Polarization properties of suspended matter for remote sensing, Appl. Opt., 40(15), 2398-2416, https://doi.org/10.1364/AO.40.002398, 2001.

Chami, M., Lafrance, B., Fougnie, B., Chowdhary, J., Harmel, T., and Waquet, F.: OSOAA: A vector radiative transfer model of coupled atmosphere-ocean system for a rough sea surface application to the estimates of the directional variations of the water leaving reflectance to better process multi-angular satellite sensors data over the ocean, Opt. Express, 23(21), 27829-27852, https://doi.org/10.1364/OE.23.027829, 2015.

Freidenreich, S. M., and Ramaswamy, V.: A new multiple-band solar radiative parameterization for general circulation models, J. Geophys. Res.-Atmos., 104(D24), 31389–31409, https://doi.org/10.1029/1999JD900456, 1999.

Gassó, S. and Knobelspiesse, K. D.: Circular polarization in atmospheric aerosols, Atmos. Chem. Phys., 22, 13581–13605, https://doi.org/10.5194/acp-22-13581-2022, 2022.

Han, Y., Ding, L., Wang, Y., Zheng, H., and Fang, L.: Polarized light illuminated scattering characteristics of single airborne particle, J. Quant. Spectrosc. Radiat. Transfer, 266, 107568, https://doi.org/10.1016/j.jqsrt.2021.107568, 2021.

Haspel, C. and Hefets, Y.: Black carbon scatterer input for scattering calculations, Zenodo [data set], https://doi.org/10.5281/zenodo.19041638, 2026.

Haspel, C., Zhang, C., Wolf, M. J., Cziczo, D. J., and Sela, M.: Measurements and calculations of enhanced side- and back-scattering of visible radiation by black carbon aggregates, Atmos. Chem. Phys., 23, 10091–10115, https://doi.org/10.5194/acp-23-10091-2023, 2023.

Hefets, Y. and Haspel, C.: Flexible scattering order formulation of the discrete dipole approximation, Appl. Opt., 62, 6093-6105, https://doi.org/10.1364/AO.496245, 2023.

Hefets, Y. and Haspel, C.: Shift of the linear polarization angle of light scattered by anisotropic aerosol and hydrosol particles, J. Quant. Spectrosc. Radiat. Transfer, 346, 109593, https://doi.org/10.1016/j.jqsrt.2025.109593, 2025.

Hefets, Y. and Haspel, C.: Single scattering code for a flexible scattering order formulation of the discrete dipole approximation, Zenodo [code], https://doi.org/10.5281/zenodo.18995083, 2026a.

Hefets, Y. and Haspel, C.: Monte Carlo of light multi-scattering code, Zenodo [code], https://doi.org/10.5281/zenodo.19043053, 2026b.

Joseph, J. H., Wiscombe, W. J., and Weinman, J. A.: The delta-Eddington approximation for radiative flux transfer, J. Atmos. Sci, 33, 2452-2459, https://doi.org/10.1175/1520-0469(1976)033%3C2452:TDEAFR%3E2.0.CO;2, 1976.

Kahnert, M. and Kanngießer, F.: Modelling optical properties of atmospheric black carbon aerosols, J. Quant. Spectrosc. Radiat. Transfer, 244, 106849, https://doi.org/10.1016/j.jqsrt.2020.106849, 2020.

Koestner, D., Stramski, D., and Reynolds, R. A.: Polarized light scattering measurements as a means to characterize particle size and composition of natural assemblages of marine particles, Appl. Opt., 59(27), 8314-8334, https://doi.org/10.1364/AO.396709, 2020.

Leighton, H.G.: Application of the delta-Eddington method to the absorption of solar radiation in the atmosphere, Atmos.-Ocean, 18(1), 43-52, https://doi.org/10.1080/07055900.1980.9649076, 1980.

Liou, K.N., Takano, Y., and Yang, P.: Intensity and polarization of dust aerosols over polarized anisotropic surfaces, J. Quant. Spectrosc. Radiat. Transfer, 127, 149-157, https://doi.org/10.1016/j.jqsrt.2013.05.010, 2013.

Liu, L. and Mishchenko, M. I.: Effects of aggregation on scattering and radiative properties of soot aerosols, J. Geophys. Res.-Atmos, 110, D11211, https://doi.org/10.1029/2004JD005649, 2005.

Liu, L. and Mishchenko, M. I.: Scattering and radiative properties of complex soot and soot-containing aggregate particles, J. Quant. Spectrosc. Radiat. Transfer, 106, 262-273, https://doi.org/10.1016/j.jqsrt.2007.01.020, 2007.

Liu, L. and Mishchenko, M. I.: Scattering and radiative properties of morphologically complex carbonaceous aerosols: A systematic modeling study, Remote Sens., 10, 1634, https://doi.org/10.3390/rs10101634, 2018.

Liu, L., Mishchenko, M. I., and Arnott, W. P.: A study of radiative properties of fractal soot aggregates using the superposition T-matrix method, J. Quant. Spectrosc. Radiat. Transfer, 109, 2656-2663, https://doi.org/10.1016/j.jqsrt.2008.05.001, 2008.

Mackowski, D. W.: Electrostatics analysis of radiative absorption by sphere clusters in the Rayleigh limit: Application to soot particles, Appl. Optics, 34, 3535–3545, https://doi.org/10.1364/AO.34.003535, 1995.

https://doi.org/10.5194/egusphere-2026-1619
Preprint. Discussion started: 6 May 2026

Mackowski, D. W.: A simplified model to predict the effects of aggregation on the absorption properties of soot particles, J. Quant. Spectrosc. Ra., 100, 237–249, https://doi.org/10.1016/j.jqsrt.2005.11.041, 2006.

Mishchenko, M. I., Hovenier, J. W., and Travis, L. D. (Eds.): Light scattering by Nonspherical Particles, Theory, Measurements, and Applications, Academic Press, ISBN 978-0124986602, 2000.

Quinby-Hunt, M. S., Erskine, L. L., and Hunt, A. J.: Polarized light scattering by aerosols in the marine atmospheric boundary layer, Appl. Opt., 36, 5168-5184, https://doi.org/10.1364/AO.36.005168, 1997.

Quinby-Hunt, M. S., Hull, P. G., and Hunt, A. J.: Polarized Light Scattering in the Marine Environment, in: Light Scattering by Nonspherical Particles: Theory, Measurements, and Applications, edited by: Mishchenko, M. I., Hovenier, J. W., and Travis , L. D., 525-553, Academic Press, San Diego, 10.1088/0957-0233/11/12/705, 2000.

Ramella-Roman, J. C., Prahl, S. A., and Jacques, S. L.: Three Monte Carlo programs of polarized light transport into scattering media: part I, Opt. Express, 13, 4420-4438, https://doi.org/10.1364/OPEX.13.004420, 2005.

Romshoo, B., Müller, T., Pfeifer, S., Saturno, J., Nowak, A., Ciupek, K., Quincey, P., and Wiedensohler, A.: Optical properties of coated black carbon aggregates: numerical simulations, radiative forcing estimates, and size-resolved parameterization scheme, Atmos. Chem. Phys., 21, 12989–13010, https://doi.org/10.5194/acp-21-12989-2021, 2021.

Romshoo, B., Pöhlker, M., Wiedensohler, A., Pfeifer, S., Saturno, J., Nowak, A., Ciupek, K., Quincey, P., Vasilatou, K., Ess, M. N., Gini, M., Eleftheriadis, K., Robins, C., Gaie-Levrel, F., and Müller, T.: Importance of size representation and morphology in modelling optical properties of black carbon: comparison between laboratory measurements and model simulations, Atmos. Meas. Tech, 15, 6965–6989, https://doi.org/10.5194/amt-15-6965-2022, 2022.

Soewono, A. and Rogak, S. N.: Morphology and Optical Properties of Numerically Simulated Soot Aggregates, Aerosol Sci. Tech., 47, 267-274, https://doi.org/10.1080/02786826.2012.749972, 2013.

Stachurski, Z. H.: Definition and properties of ideal amorphous solids, Phys. Rev. Lett. 90, 155502, https://doi.org/10.1103/PhysRevLett.90.155502, 2003.

Stachurski, Z. H.: On structure and properties of amorphous materials, Materials, 4, 1564–1598, https://doi.org/10.3390/ma4091564, 2011.

Stachurski, Z. H.: A theoretical model of an ideal amorphous solid, Physcs. Proc., 48, 55–58, https://doi.org/10.1016/j.phpro.2013.07.009, 2013.

Tyo, J. S., Goldstein, D. L., Chenault, D. B., and Shaw, J. A.: Review of passive imaging polarimetry for remote sensing applications, Appl. Opt., 45(22), 5453-5469, https://doi.org/10.1364/AO.45.005453, 2006.

Ugolnikov, O.S., Postylyakov, O.V., and Maslov, I. A.: Effects of multiple scattering and atmospheric aerosol on the polarization of the twilight sky, J. Quant. Spectrosc. Radiat. Transfer, 88, 233-241, https://doi.org/10.1016/j.jqsrt.2003.12.033, 2004.

van der Laan, J. D., Wright, J. B., Kemme, S. A., and Scrymgeour, D. A.: Superior signal persistence of circularly polarized light in polydisperse, real-world fog environments, Appl. Opt., 57, 5464-5473, https://doi.org/10.1364/AO.57.005464, 2018.

Wiscombe, W. J., and Evans, J. W.; Exponential-sum fitting of radiative transmission functions, J. Comput. Phys., 24(4), 416-444, https://doi.org/10.1016/0021-9991(77)90031-6, 1977.

Xu, M. and Alfonso, R. R.: Circular polarization memory of light, Phys. Rev. E, 72, 06560, https://doi.org/10.1103/PhysRevE.72.065601m, 2005.

Zhang, C., Zhang, Y., Wolf, M. J., Nichman, L., Shen, C., Onasch, T. B., Chen, L., and Cziczo, D. J.: The effects of morphology, mobility size, and secondary organic aerosol (SOA) material coating on the ice nucleation activity of black carbon in the cirrus regime, Atmos. Chem. Phys., 20, 13957–13984, https://doi.org/10.5194/acp-20-13957-2020, 2020.